Nighttime smoke aerosol optical depth over U.S. rural areas: first retrieval from VIIRS moonlight observations

Meng Zhou[a,b,*], Jun Wang[a,b,c,*], Xi Chen[b,c], Xiaoguang Xu[d], Peter R. Colarco[e], Steven D. Miller[f], Jeffrey S. Reid[g], Shobha Kondragunta[h], David Matthew Giles[e], Brent Holben[e]

a. Interdisciplinary Graduate Program in Geo-Informatics, The University of Iowa, Iowa City, IA 52242, USA
b. Center for Global and Regional Environmental Research, and Iowa Technology Institute, The University of Iowa, Iowa City, IA 52242, USA
c. Department of Chemical and Biochemical Engineering, The University of Iowa, Iowa City, IA 52242, USA
d. Joint Center for Earth Systems Technology, University of Maryland – Baltimore County, 1000 Hilltop Circle, Baltimore, MD 21250, USA
e. NASA Goddard Space Flight Center, Greenbelt, MD 20771, USA
f. Cooperative Institute for Research in the Atmosphere, Colorado State University, Fort Collins, CO 80523, USA
g. Marine Meteorology Division, Naval Research Laboratory, Monterey, CA 93943, USA
h. Center for Satellite Applications and Research, National Oceanic and Atmospheric Administration, National Environmental Satellite, Data, and Information Service, College Park, MD 20740, USA
*Correspondence:
Jun Wang, jun-wang-1@uiowa.edu; Meng Zhou, meng-zhou-1@uiowa.edu

Submission to
Remote Sensing of Environment
April 2021
Revised, August 2021

Abstract

An algorithm for retrieving nighttime aerosol optical depth (AOD) from the Visible Infrared Imaging Radiometer Suite (VIIRS) Day-Night Band (DNB) observations of reflected moonlight is presented for rural areas during the western U.S. fire seasons. The algorithm uses the UNified and Linearized Vector Radiative Transfer Model with newly developed capabilities for considering lunar illuminations. Cloud and fire pixels are screened out by utilizing the radiance from the VIIRS Moderate-resolution Bands and the DNB. Rural and city pixels are classified based on a pre-calculated city light database. The surface spectral reflectance for DNB ranging from 342 to 1107 nm is estimated by a random forest approach, which is trained using the surface spectral reflectance from the existing spectral libraries. For the fire seasons of 2017 and 2020, the nighttime AOD retrieval is shown to play an indispensable role in describing the nonlinear diurnal movement of smoke transport and discerning the source of smoke plumes heretofore observable only in the daytime. The retrieved AOD values show good agreement with spatiotemporally collocated Aerosol Robotic Network and Cloud-Aerosol Lidar with Orthogonal Polarization AOD values, with linear correlation coefficient values of ~0.96/0.95 and ~86%/69% of the AOD pairs falling in an uncertainty envelope of ± (0.085+0.10AOD), which is superior to AOD reanalysis from MERRA-2. These results affirm the significant potential of nighttime AOD to improve the analysis and forecast of regional to global biomass-burning aerosol distributions, filling a critical gap in the diurnal description of a critical element of Earth's climate system.

1. Introduction

The accurate characterization of the spatiotemporal distribution of aerosol particles is important for reducing uncertainties in both the estimation of climate radiative forcing and the assessment of surface air quality. Indeed, previous studies indicate that the net global radiative forcing of aerosol particles in terms of both direct and indirect effects can vary from -0.1 to -1.9 Wm^{-2} (Boucher et al., 2013), suggesting they may partially offset the carbon dioxide global warming effects of 1.82 ± 0.19 W/m^2 (Myhre et al., 2013). Furthermore, high concentrations of surface particulate matter (PM) can cause adverse health effects such as respiratory and cardiovascular diseases in humans (Pope & Dockery, 2006). A recent study shows that the PM2.5-attributable mortality rate ranges from 13 to 125 with a median of 39 per 100000 people (Anenberg et al., 2019), equivalent to ~0.039%, which is greater than the varicella fatality rate of ~0.02% for adults (Heymann, 2008). Because atmospheric aerosols have a crucial role in climate prediction and human health (Pöschl, 2005), satellite remote sensing of aerosols – the only means for quantitatively characterizing spatiotemporal variations of aerosol properties globally – has been the focus of continuous development, with steady progress made over the past three decades.

As one of the most important optical parameters for characterizing the distribution of atmospheric aerosols, aerosol optical depth (AOD) is routinely retrieved from various space-borne sensors and then assimilated into or integrated with chemistry transport models for applications such as atmospheric composition forecast or reanalysis (Sessions et al., 2015), surface air quality monitoring, visibility assessments (Hu et al., 2014; Kessner et al., 2013; Randles et al., 2017; van Donkelaar et al., 2006; Wang & Christopher, 2003; Wang et al., 2004; Xian et al., 2019), aerosol-attributable mortality estimation (Hu, 2009; Hu & Rao, 2009; Kloog et al., 2011), and long-term

climate change studies, etc. Currently, daily *global* AOD products are routinely obtained via instruments such as the Moderate Resolution Imaging Spectroradiometer (MODIS) (Hsu et al., 2004; Levy et al., 2003; Lyapustin et al., 2011; Wang et al., 2017) and the Visible Infrared Imaging Radiometer Suite (VIIRS, Hsu et al., 2019; Sawyer et al., 2020; Huang et al., 2016; Jackson et al., 2013; Liu et al., 2014) onboard polar orbiting satellites. However, these products are often reported for daytime AOD at the synoptic observing times of these sun-synchronous satellites, namely 1030 local time (Terra MODIS) or 1330 local time (Aqua MODIS and SNPP VIIRS, NOAA20 VIIRS), leaving a 20-hour gap devoid of AOD retrievals over the tropical to mid-latitude regions where most of the human population resides. Because geostationary satellites can constantly monitor the same earth view at a relatively high temporal frequency, efforts have been made to derive AOD from geostationary satellite observations (Liu et al., 2008; Lee et al., 2010; Thieuleux et al., 2005; Wang et al., 2003b; Zhang et al., 2011; Zhang et al., 2013; Zhang et al., 2018, Huff et al., 2021). AOD products from the Geostationary Ocean Color Imager and the Geostationary Operational Environmental Satellite R-series are routinely generated. However, uncertainties when retrieving AOD from geostationary satellites should be further quantified as a function of aerosol model assumption, view geometry, and cloud contamination (Zhang et al., 2011; Zhang et al., 2018). Despite the benefits of increased temporal sampling, there remains a lack of routine characterization of global AOD distribution at nighttime due to the corresponding lack of sensitivity of infrared measurements to fine-mode aerosol size distributions. These issues can be overcome, in part, by leveraging novel low-light visible observations capable of sensing faint signals of visible light from moonlight at night.

Nighttime AOD product is needed to supplement daytime AOD products from existing sensors to describe the diurnal variation of AODs for several important reasons. First, reliable nighttime aerosol observations can help the communities better understand the role of aerosols in atmospheric chemistry. With the absence of sunlight, the nocturnal chemical evolutions of aerosol and trace gases are far different from their daytime counterparts (Wang et al., 2016). The shallow boundary layer and weak turbulent mixing suppress the dispersion of nighttime emissions such as those from power plants. The higher nocturnal concentration of aerosols in the surface layer can thus trigger significant and complex chemical processing and form aerosols that are relevant to air quality, regional haze, fog, and climate issues. Although efforts have been made to study the diurnal variation and corresponding impact of aerosols (Lennartson et al., 2018; Reid et al., 2017), these analyses have mostly relied on ground observation or model simulation for nighttime AOD. Therefore, nighttime AOD retrieved from satellites can provide much-needed constraints for quantifying aerosol loading and evolution at all times. Second, assimilation of nighttime aerosol observations such as AOD into an air pollution forecast model has the potential to further enhance the model's forecasting skill. Multiple studies show that aerosol assimilation techniques such as the 2D/3D variational technique and 4D Var adjoint method can improve the accuracy of the model forecast (Adhikary et al., 2008; Sekiyama et al., 2010; Wang et al., 2013; Wang et al., 2012; Xu et al., 2013; Zhang et al., 2008). However, to achieve this goal, a minimum of 12 hours of observation is required, which means that nighttime observation is potentially valuable as a gap filler in most assimilation applications (Singh et al., 2019). Third, in high-latitude regions such as Alaska, MODIS AOD is available on less than 10% of the days per year due to the low solar zenith angles and long winter-season nights. Thus, applications of AOD for mapping surface $PM_{2.5}$ concentrations are dramatically limited in high-latitude regions where climate sensitivity and

associated indicators of climate change are high (Myhre et al., 2013; Konya et al., 2021). Nighttime AOD, therefore, is important for $PM_{2.5}$ mapping since the daily air quality standards for $PM_{2.5}$ are often expressed in terms of surface dry $PM_{2.5}$ mass concentration at 24-h averages (Wang et al., 2016). Information about nighttime $PM_{2.5}$ can better constrain the representation of the daily-mean PM concentration and thus the assessment of the surface air quality (Fu et al., 2018).

A few studies have attempted to retrieve AOD at night from the VIIRS Day-Night Band (DNB), but they concentrated on the measurements of city lights from space and did not use the back-scattered moonlight at night. For example, Johnson et al. (2013), Zhang et al. (2019), and studies cited therein explored the capability of nighttime AOD retrieval over urban regions using city lights observed by VIIRS DNB. In parallel, Wang et al. (2016) and Fu et al. (2018) investigated the correlation of the DNB observations and surface PM2.5 at the urban scale. Although progress is continuously being made, the limitations of these studies lie in their assumptions when relating AOD to DNB observation. For example, multiple scattering and gas absorption are neglected in these algorithms, as is the surface reflection of city light (Wang et al., 2020b). In addition, the spatial scale of these studies is limited to urban areas, leaving vast rural regions unexplored.

Here, we develop a new technique to significantly improve AOD availability at night from passive satellite remote sensing techniques by using the back-scattered moonlight over rural areas (i.e., away from city light emissions, which present a source of contamination to this technique). This work is the first in a series of studies to demonstrate the potential of the VIIRS DNB for nighttime AOD retrieval and air quality applications over rural and remote areas removed from dominant city light sources. As the first demonstration, our development of the retrieval algorithm

141 strategically focuses on pollution events caused by North American smoke transport that
142 frequently affects air quality in rural areas; in these cases, the strong signal of aerosol backscatter
143 favors the retrieval of AOD that has large spatial and temporal variations at night as a result of
144 long-range transport. To simulate the moonlight measured by DNB, the algorithm uses the latest
145 UNified and Linearized Vector Radiative Transfer Model (UNL-VRTM, Wang et al., 2014) that
146 has been applied to multiple designs of satellite mission concepts and retrieval algorithms for
147 remote sensing of aerosols (Ding et al., 2016; Hou et al., 2017; Xu & Wang, 2015; Xu et al., 2019;
148 Xu et al., 2015). The latest development allows UNL-VRTM to conduct nighttime radiative
149 transfer calculation by including additional source functions to treat illumination from the Moon,
150 fires, and artificial lights (Wang et al., 2020b).
151
152 This paper is structured as follows. Section 2 provides a brief overview of VIIRS DNB and the
153 datasets used in this work, as well as the study area and time period. Section 3 details the nighttime
154 AOD retrieval scheme, and Section 4 provides an assessment of retrieval results with Aerosol
155 Robotic Network (AERONET) and Cloud-Aerosol Lidar with Orthogonal Polarization (CALIOP)
156 data and compares them to the re-analysis of AOD from Modern-Era Retrospective analysis for
157 Research and Applications, version 2 (MERRA-2). Sensitivity analysis with respect to the key
158 parameters of the retrieval framework is also conducted in this section. Finally, Section 5
159 summarizes the paper.
160

161 **2. Data, Data Processing, and Model**

162 The nocturnal AOD algorithm is designed to use VIIRS nighttime observation (Section 2.1) to
163 retrieve AOD through a look-up-table (LUT) approach that is generated using the UNL-VRTM

(Section 2.4) radiative transfer code. AERONET data (Section 2.2) and other data (such as MODIS MAIAC AOD, MERRA-2 data, and CALIOP data, as in Section 2.3) are also used to evaluate the retrieval.

2.1. VIIRS nighttime observation

Carried onboard the polar-orbiting satellites Suomi-NPP and NOAA-20 (also referred to as the Joint Polar Satellite System-1, or JPSS-1), VIIRS is the latest generation of operational moderate resolution imager following the legacy of the Advanced Very High Resolution Radiometer (AVHRR) of the National Oceanic and Atmospheric Administration (NOAA) and MODIS on the National Aeronautics and Space Administration's (NASA) Terra and Aqua satellites. VIIRS images Earth in 22 bands with a nominal spatial resolution of 375 m in its five imagery bands (I-bands), 750 m in its sixteen moderate-resolution bands (M-bands) and the DNB, and 742 m in its special DNB low-light visible sensor. VIIRS DNB (Miller et al., 2013) is a panchromatic band in the visible and near-infrared spectrum (342 ~ 1107 nm). The wide dynamic range (from 3×10^{-9} to 0.02 W cm^{-2} sr^{-1}) of the DNB gives it the ability to detect low light such as reflected lunar radiances at night. Detailed information about the VIIRS sensor can be found in elsewhere in the literature (Elvidge et al., 2017; Lei et al., 2020; Liao et al., 2013; Polivka et al., 2015; Wolfe et al., 2013).

We obtained the VIIRS Suomi NPP Level-1B calibrated DNB radiance data (VNP02DNB) (Chen et al., 2017) and the DNB geolocation product (VNP03DNB) from the NASA Level-1 and Atmosphere Archive & Distribution System (LAADS) (https://ladsweb.modaps.eosdis.nasa.gov/). We also obtained the corresponding Level-1B calibrated M-band radiance product (VNP02MOD) and geolocation product (VNP03MOD) for cloud masking (Section 3.3). The VIIRS Black Marble

product (VNP46A1, Román et al., 2018) was used for an artificial city light mask. It should be noted that all VIIRS products used in this study are for nighttime only. Although Level-1B products have undergone vigorous calibration processes to correct the contamination from various sources such as stray light (Mills et al., 2013; Shao et al., 2018), subsequent studies have shown that residual contaminations can remain in Level-1B. To obtain better data quality in this study, we considered only the pixels whose quality flags are equal to 0 (e.g., best quality) to minimize data uncertainty associated with the sensor itself. For example, this quality threshold will exclude pixels with missing or corrupted calibration data as well as pixels that are contaminated by stray light and those that are saturated.

2.2. AERONET AOD and Aerosol Properties

AERONET is a network of autonomously operated Cimel Electronique Sun-sky photometers used to measure Sun collimated direct beam irradiance (at 440 nm, 670 nm, 870 nm, 940 nm, and 1020 nm) and directional sky radiance, which provides scientific-quality column-integrated aerosol properties of AOD and aerosol microphysical and radiative properties. Since 1993, when AERONET began to collect daytime aerosol information, the number of AERONET sites has continuously increased; there were more than 500 active sites as of 2019 (Giles et al., 2019). In 2015, AERONET began to extend its measurements to nighttime, deriving AOD using the Moon as the light source (Barreto et al., 2016; Berkoff et al., 2011; Giles et al., 2019b). Currently, there are ~200 AERONET sites reporting nighttime lunar-based AOD. This research uses officially released AERONET Level 2.0 Version 3 (V3) Aerosol Inversion products to define the aerosol model for the radiative transfer simulation. AEROSOL OPTICAL DEPTH (V3)-SOLAR and LUNAR AOD (V3)-PROVISIONAL were used to evaluate the DNB retrievals. The AERONET

V3 dataset is now available on the AERONET web site (https://aeronet.gsfc.nasa.gov). It should be noted that AERONET radiance measurement at night have no absolute calibration, but rather relies on the relative transformation of the daytime calibration coefficient to the nighttime (Li et al., 2016). The total calibration uncertainty ranges from 5% to 12% depending on wavelength (greatest for 1640 nm) and lunar phase angle (greatest for 90 degrees). While the present estimated nighttime AOD uncertainty is approximately 0.03, the current nighttime AOD products may also have significant cloud contamination, introducing additional bias (Giles et al., 2019a). As a result, the AERONET V3 nighttime data set is currently considered "provisional" Level 1.5 due to ongoing development to improve the instrument's nighttime calibration, cloud screening, and quality controls. Due to the changing nature of the current data set, the AERONET V3 data used for this study are provided as a supplement.

For this study, we evaluated the nighttime AOD derived from VIIRS DNB at 550 nm against both intra-day interpolated (τ_{AID}) and nighttime (lunar)-based (τ_{LNR}) AERONET AOD retrievals (V3 AOD products, both daytime and nighttime). To make the validation comparable, we firstly used the Angstrom exponent (AE) provided to interpolate AERONET AOD to 550 nm. While τ_{LNR} is directly measured at night, for those not having nighttime lunar measurements, τ_{AID} at nighttime is obtained via interpolation. Specifically, for the nighttime dataset, a one-hour temporal window was used to acquire the mean τ_{LNR} at the VIIRS overpass time. To ensure the data quality, a minimum of two measurements within the one-hour window are required. For the daytime dataset, AOD measurements were firstly aggregated into the hourly level using the same data quality control criterion. Then, a 20-hour temporal window was used to acquire the two nearest daytime AOD measured on the following morning and the previous afternoon. Hence, for a nominal VIIRS

233 nighttime overpass of 0130 local time, the allowed time window is 1530 on the previous afternoon
234 and 1130 in the following morning. Then, the τ_{AID} is obtained by interpolation linearly from the
235 two closest daytime AOD value points in the time domain to the satellite overpass time.
236
237 *2.3. Other data*
238 We used Multi-Angle Implementation of Atmospheric Correction (MAIAC) AOD (MCD19A2,
239 Lyapustin et al., 2011) for spatial comparison with the DNB retrieval results. The MODIS MAIAC
240 product is valid during the daytime only and is used here as a reference to qualitatively estimate
241 the general spatial distribution of DNB-retrieved AOD at night. Furthermore, to obtain the surface
242 albedo that is needed as the boundary condition for the AOD retrieval from DNB, we derived a
243 monthly climatology of the surface bidirectional reflectance distribution function (BRDF) from
244 ten years of MODIS MAIAC spectral BRDF/albedo product (MCD19A3). MCD19A3 provides
245 three coefficients (for the isotropic, volumetric, and geometric kernels, respectively) derived from
246 the Ross-Thicke Li-Sparse (RTLS, Wanner et al., 1995) BRDF model for MODIS bands 1 through
247 8, representing cloud-free and low aerosol conditions. A monthly climatology of the RTLS
248 parameter is obtained by averaging the corresponding coefficient in the same month from the past
249 ten years' records. MODIS MAIAC products are generated on the 1 km sinusoidal grid.
250
251 Nighttime aerosol measurements from CALIOP (Getzewich et al., 2016), specifically the CALIOP
252 Level 2 (Version 4.10) 5 km aerosol layer product, aboard the Cloud-Aerosol Lidar Infrared
253 Pathfinder Satellite Observations (CALIPSO) spacecraft was used to validate the DNB AOD
254 retrieval. Column AOD at 532 nm with 5 km resolution was obtained by integrating the aerosol
255 extinction coefficients along the altitude.

Assimilated meteorological (Gelaro et al., 2017) and aerosol (Randles et al., 2017; Buchard et al., 2017) fields were used from the MERRA-2. MERRA-2 meteorological fields (M2T3NVASM) were used to provide the ground temperature as the ancillary information needed for detecting cloudy pixels in VIIRS DNB data. The MERRA-2 AOD analysis (M2I3NXGAS) data were also used as the baseline to evaluate the added value of the DNB retrieval; the DNB retrieval should be better than those model simulations when it comes to agreement with AERONET and CALIOP nighttime AOD if they are to be deemed useful for future model forecast and evaluation. The spatial resolution of the MERRA-2 dataset is 0.5º×0.625º in 72 hybrid sigma/pressure levels, and its temporal resolution is 3 hours. Surface temperature and AOD were first linearly interpolated to the DNB overpass time. Then, for surface temperature, a bi-linear interpolation was used to interpolate the temperature to DNB grids.

2.4. Nighttime UNL-VRTM

As mentioned earlier, the UNL-VRTM comprises seven modules: (1) a vector linearized radiative transfer model (Spurr & Christi, 2019; Wang et al., 2014; Xu & Wang, 2019), (2) a linearized Mie scattering code (Spurr et al., 2012), (3) a linearized T-matrix electro-magnetic scattering code (Spurr et al., 2012), (4) a surface BRDF and bi-directional polarization function (BPDF) module, (5) a module that computes Rayleigh scattering and gas absorption (using HITRAN and other molecular absorption cross-section databases), and (6-7) two modules for the analysis—an optimal inversion code and a visualization tool for diagnosis. The latest developments incorporate (a) a spectrally resolved moon-phase-based lunar irradiance model developed by Miller and Turner (2009); (b) an astrophysical code (Schlyter, 2010) that computes geometrical configurations

(zenith and azimuth angles as well as the moon phase angle, earth-moon distance, and sun-moon distance) of any given time and any given location on Earth; (c) an extension of the representation of the surface emission at the bottom layer of the atmosphere by adding a Planck function-based term for fire radiative emission sources and a spectral-based term for modern artificial lamps (Wang et al., 2020b). These new features empower the UNL-VRTM to simulate the light transfer of nighttime scenarios, such as the backscattered radiation fields illuminated by the Moon as a function of moon phase, as well as the upwell radiance of artificial light or fires. Comparison with moonlight measured at NASA Jet Propulsion Laboratory (JPL) shows that the uncertainty of the UNL-VRTM simulated transfer of moonlight is within $\pm 10\%$ (Wang et al., 2020b).

3. Nighttime AOD retrieval algorithm

Figure 1 illustrates the procedure for processing VIIRS DNB data and the subsequent retrieval of the nighttime AOD. Briefly, the retrieval algorithm entails the following steps:

1) Calculate the TOA reflectance of the DNB from the Level-1B DNB radiance (Section 3.1) and the lunar irradiance model.
2) Estimate the surface reflectance for the DNB observation (Section 3.2).
3) Identify the VIIRS pixels that are suitable for the AOD retrieval. Water body, cloud, fire, and urban areas are excluded through various tests in this step (Section 3.3).
4) Invert the classified TOA reflectance of DNB from a pre-calculated LUT to obtain AOD (Section 3.4).

We describe each of these in the sections below.

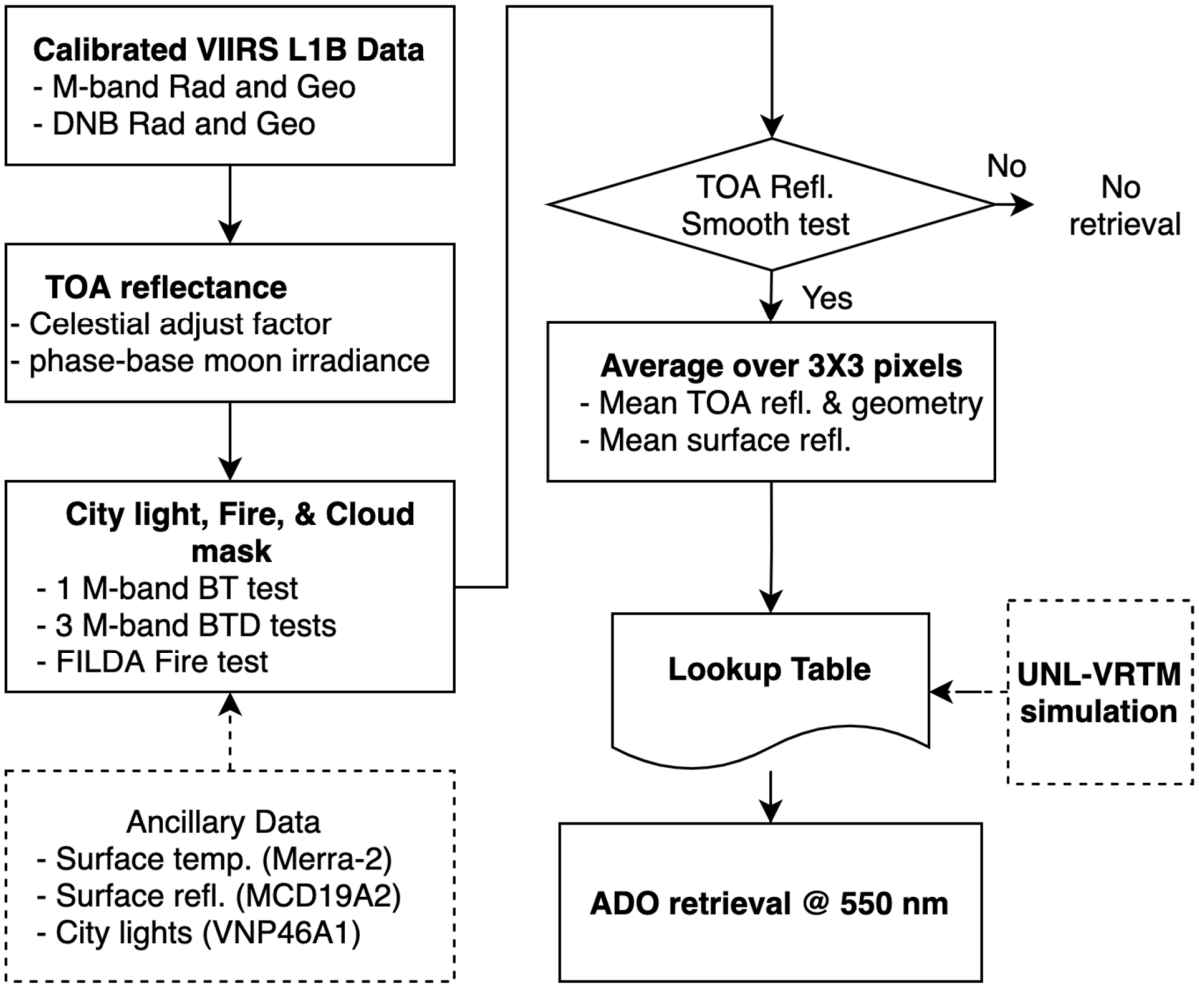

Figure 1. Flowchart of the nighttime AOD retrieval scheme

3.1. Obtain the TOA reflectance

As stated earlier, DNB is a panchromatic band ranging from 342 nm to 1107 nm. The prelaunch DNB relative spectral response (RSR) function was carefully designed to monitor the red and near infrared NIR light with more weights on the NIR to minimize atmospheric (Rayleigh) scatter contamination. However, the centroid of the actual RSR after launch shifted slightly to the blue, and the full width at half maximum decreased slightly because of the degrading of the mirror coatings. The postlaunch DNB RSR can be obtained from the NOAA STAR Calibration center

online: https://ncc.nesdis.noaa.gov/VIIRS/VIIRSSpectralResponseFunctions.php. It provides the relative response function for 16 sets of detectors and 52 wavelengths ranging from 342 nm to 1107 nm (in total 832 digital numbers). With the RSR, the TOA DNB reflectance values are calculated as:

$$\rho_{\mathrm{DNB}}^{\mathrm{TOA}} = \frac{\pi I_{\mathrm{DNB}}}{\mu_0 \alpha_t \int_{\lambda_2}^{\lambda_1} f_{\mathrm{RSR}}(\lambda) E_{1\mathrm{AU}}^{\mathrm{TOA}}(\lambda, \theta_p)\, d\lambda} \quad (1)$$

where I_{DNB} is the DNB-measured radiance, $E_{1\mathrm{AU}}^{\mathrm{TOA}}(\lambda, \theta_p)$ stands for the standardized moon irradiance varying with wavelength λ and moon phase angle θ_p, $f_{\mathrm{RSR}}(\lambda)$ is the DNB RSR at wavelength λ, and μ_0 is the is the cosine of lunar zenith angle. I_{DNB} is the panchromatic radiance measured by VIIRS and can be calculated as:

$$I_{\mathrm{DNB}} = \int_{\lambda_2}^{\lambda_1} f_{\mathrm{RSR}}(\lambda) I(\lambda)\, d\lambda \quad (2)$$

where $I(\lambda)$ is the TOA radiance at each DNB sub-band. Unlike the solar irradiance, which can be viewed as nearly constant with time, the moon irradiance is determined by the geometry between the Sun, Earth, and Moon. Thus, a time-dependent adjustment factor α_t needs to be calculated, following Miller and Turner (2009) as follows:

$$\alpha_t = \left(\frac{\bar{R}_{\mathrm{se}}}{R_{\mathrm{se}}}\right)^2 \left(\frac{\bar{R}_{\mathrm{me}} - r_{\mathrm{e}}}{R_{\mathrm{me}} - r_{\mathrm{e}}}\right)^2 \quad (3)$$

where $\bar{R}_{\mathrm{se}}$ and $\bar{R}_{\mathrm{me}}$ are the mean values of Sun-Earth distance and Moon-Earth distance, respectively, r_{e} is the mean value of the earth radius, and R_{me} and R_{se} are the instantaneous Moon-Earth and Sun-Earth distances, respectively, at the satellite overpass time and are available in the VNP03DNB dataset. The standardized lunar irradiance model we used in this study was developed by Miller and Turner (2009) and has a spectrum range of 202 - 2800 nm, with a spectral resolution of 1 nm. In the UNL-VRTM, a Gaussian shape response function with a full width at half maximum (FWHM) of 15 nm (Liao et al., 2013) is used to convolve this lunar irradiance database

at a spectral resolution of 1 nm to obtain the irradiance for each of DNB (52) sub-band. The moon phase angle resolution of the dataset is one degree. A linear interpolation is used here to obtain the moon irradiance of a given moon phase at the satellite overpass time.

As shown in Eqns. (1) and (2), the differences between $\rho_{\mathrm{DNB}}^{\mathrm{TOA}}$ and the solar band reflectance that is commonly used in the daytime retrieval algorithms lie in three areas. First, assuming that other factors such as atmosphere and land properties and the satellite view angle are equal, $\rho_{\mathrm{DNB}}^{\mathrm{TOA}}$ further depends on the Sun-Earth-Moon geometry; the impact of the geometry on $\rho_{\mathrm{DNB}}^{\mathrm{TOA}}$ can be up to 15% since α_t can vary from 0.90 ~ 1.17. Second, unlike the solar band reflectance calculation in which the incoming irradiance at TOA depends on solar zenith angle only (considering solar spectral irradiance is relatively constant), $\rho_{\mathrm{DNB}}^{\mathrm{TOA}}$ calculation needs both moon phase angle and moon zenith angle to estimate the incoming irradiance at TOA from the moon. Third, $\rho_{\mathrm{DNB}}^{\mathrm{TOA}}$ is a panchromatic reflectance considering the wide spectral range of the DNB sensor, within which several strong atmospheric gas absorption bands exist, while the solar band reflectance for aerosol retrievals is often narrow-band reflectance.

3.2. Determination of the DNB surface reflectance

The estimates of surface reflectance present another challenge for aerosol retrievals. Hou et al. (2017) summarized the surface assumptions of many existing retrieval algorithms. Although varying in wavelength, the similarity of these algorithms using single-angle measurements is that they use a limited number of narrow bands (<20 nm) to retrieve the atmosphere. Thus, surface reflectance in these bands may be derived by using a prescribed relationship from the surface reflectance at other bands where aerosol effects and gas absorption are minimal (such as in the

355 MODIS Dark-Targe (DT) algorithm (Levy et al., 2003)). However, these past methods are not
356 applicable to the DNB, which has a much wider spectral band width within which surface
357 reflectance can vary significantly with wavelength. As shown in Figure 2a, the DNB covers a
358 relatively wide range of the spectrum, where a strong red edge phenomenon, defined as the
359 dramatic change of surface reflectance from visible to NIR band, occurs in active photosynthetic
360 surfaces such as vegetation and rangeland.
361
362 To obtain the surface spectral reflectance for each sub-band ($R(\lambda)$) in the DNB, a random forest
363 (RF) technique (Svetnik et al., 2003) was applied to recover the surface reflectance at 52
364 wavelengths of DNB sub-bands from the MODIS surface reflectance at 7 bands. Figure S1 in the
365 supplemental materials shows the flowchart of the surface reflectance estimation. Since it is a
366 machine-learning-based approach, it consists of two steps, namely training and application. The
367 dataset used for training the RF is the combination of the spectral surface reflectance databases
368 compiled by the United States Geological Survey (USGS) (Clark et al., 2007) and the Advanced
369 Spaceborne Thermal Emission Reflection Radiometer team (ASTER) (Baldridge et al., 2009) for
370 a wide range of surface types. In the training process, spectral surface reflectance from USGS and
371 ASTER databases were sampled to the 7 MODIS narrow bands to form the feature dataset. Spectral
372 surface reflectance data at the 52 DNB sub-bands were also sampled from the database to form the
373 label dataset. Then, feature and label datasets were fed into the RF iteratively to predict the label
374 from the feature. In essence, the RF model is trained by using the reflectance at the MODIS 7
375 bands to predict the reflectance values at the 52 DNB sub-bands. To verify the approach, 70% of
376 the USGS and ASTER dataset were used to form the training set, 15% were used to validate the
377 training process, and the remaining 15% were held back and only applied to the final assessment

of the model. Fig. 2b presents the final assessment results of the RF-based DNB spectral surface reflectance estimation. The linear correlation coefficient of 1.0 and small root mean square error (RMSE) of ~0.01 indicates that the RF can estimate the DNB spectral surface reflectance with very high accuracy. Once trained, in the application phase, 7 bands of MODIS surface BRDF were derived from the 10-yr averages of MODIS monthly surface BRDF climatology at VIIRS overpass geometries, which were subsequently fed into the RF model to predict the spectral reflectance at DNB's 52 sub-bands. However, AOD retrieval uncertainty due to the surface may remain and needs to be further qualified in future work, as currently there is no direct measurement of broadband reflectance in the spectral range of DNB.

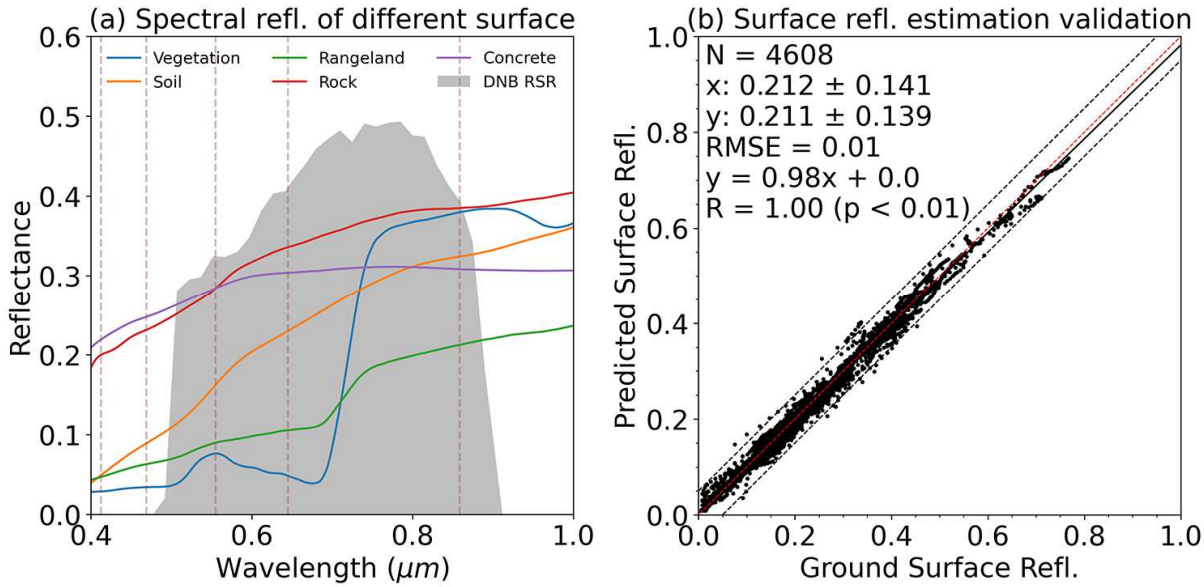

Figure 2. (a) Spectral reflectance of different land surface types. The shaded area denotes the DNB relative spectral response (RSR) function. MODIS bands within the DNB RSR are denoted as dashed brown lines and are centered at 412, 470, 550, 645, and 860 nm (from left to right). (b) Validation of the surface spectral reflectance estimated by machine-learning via the random-forest approach. The dashed line is the ± 0.05 error line.

3.3. Determination of the suitable pixels for retrieval

After acquiring the DNB TOA reflectance and the surface reflectance, the algorithm deployed a series of steps to select pixels suitable for AOD retrieval. They included the screening of pixels contaminated by artificial lights, clouds, fires, and water surfaces. For the rural region, most of which is not affected by artificial lights, moonlight is the main source of illumination and the artificial lights present a form of noise. In the study, we masked the city and artificial light pixels using a pre-calculated city light database. This city light database was derived from the three-month statistics of the black marble product VNP46A1. The nighttime light coefficient of variance, which was defined as the ratio between the three-month standard deviation of the DNB radiance and the corresponding mean, was calculated on each of the standard VNP46A1 grids. Pixels whose coefficients of variance were larger than the threshold of 0.5 are kept for possible retrieval. Like the city and artificial light, active fire also serves as noise when moonlight is used as the light source for the retrieval. Although the operational VIIRS M-band active fire detection provides near-real-time fire detection products, several studies (Polivka et al., 2016; Wang et al., 2020a) indicate that quite a few fire pixels can be missed by the operational algorithm. We also refined the M-band nighttime fire detection scheme based on our past work (Polivka et al., 2016) with the use of the DNB to detect fire light for more aggressive classification of fire pixels and subsequent removal of these pixels in the retrieval. However, it should be noted that the city and artificial light mask could only remove stable light sources such as the city light. It is hard to identify and mask transient light presented on the ground such as the traffic lights. The fire mask would only mask out the fire pixels themselves. On the other hand, the aforementioned upwell light source would potentially illuminate their adjacent dark pixels. The radius and strength of this illumination were affected by multiple factors, including but not limited to the intensity of the light source, the aerosol

417 loading, the aerosol geometric thickness, and the view geometry of DNB. In other words, the
418 current method might fail to identify dark pixels that were illuminated by diffuse radiance from
419 another surface light source. This is a limitation of the current algorithm and a direction for
420 improvement.
421
422 Using VIS and NIR channel information, conventional cloud screening algorithms identify a cloud
423 pixel by detecting the reflectance, temperature, or spatial variation caused by the presence of the
424 cloud (Saunders, 1986; Saunders & Kriebel, 1988). However, due to the lack of visible band
425 information, most of the nighttime cloud mask algorithms can only detect the cloud through
426 infrared channels. For example, four tests are adopted in the current operational VIIRS nighttime
427 cloud mask algorithm for land surface (Kopp et al., 2014), including one brightness temperature
428 test (10.76 μm) and three brightness temperature difference tests (10.76 μm - 12.01 μm, 3.7 μm -
429 12.06 μm, and 10.76 μm - 3.7 μm) in Thermal Emissive Bands. Although DNB records visible
430 light at night that could be used to help mask the cloud, the pixel footprint mismatch between DNB
431 and M-band observations is a hurdle when it comes to combining them for cloud mask in a manner
432 similar to the daytime cloud mask algorithm. Wang et al. (2020a) have developed a fast-mapping
433 method to resample observations from the DNB to the M-band. Here, this approach was applied
434 inversely to map the M-band observation to DNB, which enabled us to add two tests for further
435 screening out cloudy pixels in addition to the current operational nighttime cloud mask scheme.
436 The first one is the DNB radiance test; pixels whose DNB radiance are greater than a certain
437 threshold are flagged as cloudy pixels. Since the background radiance was affected by the moon
438 light and changed with time, the threshold used in this test was dynamically determined through a
439 histogram method (similar to our past work by Polivika et al., 2016). The second was the DNB

spatial coherence test. A spatial window of 3×3 pixels was used to test the local uniformity for a pixel. The DNB cloud tests were only applied to the rural region.

Finally, for each identified clean pixel, a 3×3 spatial window was applied to smooth the TOA reflectance. The retrieval would only be done when the number of valid pixels was greater than 4. Considering the 750 m spatial resolution of DNB, the spatial variation of aerosol in this (~2×2 km) spatial window should be relatively small. It was expected that when more pixels were used in the reflectance smoothing, the retrieval error would be smaller (although the reduction of the error is not significant, as discussed in Section 4.3).

3.4. Lookup Tables (LUTs)

The LUTs for the current retrieval consist of simulated DNB TOA reflectance for a set of AOD values under various atmospheric conditions and observation scenarios such as different view geometries, moon phases, and surface reflectances, as shown in Table 1. TOA reflectance at each DNB sub-band was first computed in UNL-VRTM with the treatment of aerosol optical properties at each corresponding band and was subsequently used to compute DNB reflectance at TOA with consideration of RSR. Details are provided by Wang et al. (2020b). Thereby, a 6D radiance data cube was generated in dimensions of the AOD, moon zenith angle, view zenith angle, scattering angle, wavelength, and surface reflectance ($N_\tau \times N_{\mathrm{mza}} \times N_{\mathrm{vza}} \times N_{\mathrm{sca}} \times N_\lambda \times N_{\mathrm{refl}}$). It should be noted that N_τ is the broadband parameter representing the reported AOD at 550 nm, while N_λ is the number of the DNB's sub-bands, and N_{refl} is the number of the surface reflectances used in the simulation. N_{mza}, N_{vza}, and N_{sca} are the geometry dimensions. When applied to retrieval, radiances from the 6D data cube were first extracted based on the view geometry to get a 3D data

cube ($N_\tau \times N_\lambda \times N_{\mathrm{refl}}$). Then, surface spectral reflectance was considered at each sub-band to extract the radiance from the 3D data cube, forming a 2D data array ($N_\tau \times N_\lambda$). Finally, TOA radiances at these DNB sub-bands were convolved with the DNB RSR to obtain the panchromatic DNB reflectance at TOA as part of the LUT. In this way, the final entry of LUT was the broadband DNB TOA reflectance as a function of the AOD with the consideration of the DNB RSR. Meanwhile, in the radiative transfer simulation, we assumed a mid-latitude summer atmospheric profile with a surface pressure of 1013 mb. In this way, the Rayleigh scattering effect was considered in the algorithm. We neglected the effects of surface pressure variation on the Rayleigh optical depth. As shown in Figure S2, although the Rayleigh optical depth varies from 0.155 at 492 nm to 0.007 at 1020 nm, Rayleigh scattering (with consideration of DNB RSR) only contributes to <0.045 optical depth over typical green surfaces in rural areas. Considering a variation of surface pressure of 20% for the land surface, which is applicable for most of the land surface, the AOD retrieval error caused by using a constant surface pressure for Rayleigh scattering estimation was within 0.01.

Table 1. Adopted parameters for generating LUTs

Dimension Name	Variable Name in Table	Number of entries	Discrete Values
Wavelength	N_λ	52	492 to 1020 nm every 15 nm
AOD at 550 nm	N_τ	20	0.00, 0.01, 0.05, 0.10, 0.15,0.20, 0.30, 0.40, 0.60, 0.80, 1.00, 1.20, 1.40, 1.60, 1.80, 2.00, 2.50, 3.00, 4.00, 5.00

Moon zenith angle	N_{mza}	21	0°, 4°, 8°, 12°, 16°, 20°, 24°, 28°, 32°, 36°, 40, 44°, 48°, 52°, 56°, 64°, 68°, 72°, 76°, 80°
Sensor zenith angle	N_{vza}	20	0°, 2.84°, 6.52°, 10.22°, 13.93°, 17.64°, 21.35°, 25.06°, 28.77°, 32.48°, 36.19°, 39.90°, 43.61°, 47.32°, 51.03°, 54.74°, 58.46°, 62.17°, 65.88°,69.59°
Scattering angle	N_{sca}	5527	Every 4° interval in the range from $180-(\theta_s+\theta_v)$ to $180-\lvert\theta_s+\theta_v\rvert$ for all pairs combination of moon zenith angle and sensor zenith angle
Surface reflectance	N_{refl}	17	0 to 0.8, with a step of 0.05

The aerosol model (Table 2) used in the radiative transfer calculation consisted of the volume media radius and effective variance for both coarse and fine modes, the fine mode fraction, and a refractive index of 440, 675, 870, and 1020 nm. They were derived by a cluster analysis (Omar et al., 2005; Xu & Wang, 2015) of the AERONET V3 Level 2.0 retrievals during three fire seasons (July to October for 2017, 2018, and 2020) over the continental U.S (Sinyuk et al., 2020). We intentionally excluded 2019 since there were no significant fire events that year. As part of the AERONET inversion products, optical parameters, including the volume median radius and the effective variance for both the coarse mode and fine mode of the aerosol, as well as the fine mode fraction, were binned together in our analysis by increments of 0.1 in 675 nm AOD (τ_{675}). Then, to achieve the best fit, either linear or logarithm regression was applied to each aforementioned parameter using τ_{675} as the reference variable; the results are that the aerosol size distribution parameters and fine-mode fraction can be modeled dynamically as a function of AOD (Remer et

al., 2005). Note that Level 2.0 data has a minimum 440 nm AOD threshold of 0.4 for single scattering albedo (SSA). Hence, in the regression process, we included the SSAs for AODs that are less than 0.4 from the AERONET Level 1.5 dataset. Although it may introduce additional bias, the SSA dynamic model would only provide qualitative knowledge of the SSA variability with the AOD. As shown in Figure S3, the SSA of the aerosol model varies from 0.93 at conditions of very low AOD of ~0.1 to 0.98 at the polluted condition of AOD up to 3; this indicates that aerosol released by the biomass burning enhanced the scattering of the light.

Table 2. Aerosol Model

Parameter Name	Short Name	Value
Volume Median Radius (Coarse Model)	VRM-C	$0.24204\tau + 3.3714$
Effective variance (Coarse Model)	V_{eff}-C	$-0.03067\tau + 0.63419$
Volume Median Radius (Fine Model)	VRM-F	$0.01335\tau + 0.2055$
Effective variance (Fine Model)	V_{eff}-F	$0.00764\tau + 0.42631$
Fine mode fraction	FMF	$0.0523 \ln \tau + 0.94101$
Real art of refractive index	M_r	1.53
Imaginary art of refractive index (440 nm)	M_{i440}	$-0.00092 \ln \tau + 0.00901$
Imaginary art of refractive index (675 nm)	M_{i675}	$-0.00118 \ln \tau + 0.00750$
Imaginary art of refractive index (870 nm)	M_{i870}	$-0.00209 \ln \tau + 0.00686$
Imaginary art of refractive index (1020 nm)	M_{i1020}	$-0.00268 \ln \tau + 0.00642$

The process for prescribing refractive index need elaboration. Since the imaginary part of the refractive index (m_i) has strong wavelength dependence, its value at 52 sub-bands of DNB were computed based on the refractive index at 440 nm, 675 nm, 870 nm, and 1020 nm. Specifically, a

two-dimensional cubic interpolation in both wavelength and AOD was applied to derive the imaginary part of the refractive index at every DNB sub-band. As in the SSA, the Level 2.0 dataset does not contain m_i retrievals for AOD less than 0.4, and we included this portion of data from the Level 1.5 dataset. For 675 nm, the m_i ranges from 0.01 to 0.006 as AOD increases, making the aerosol model dimmer than the DT non-absorbing aerosol model of 0.007 when AOD is low and brighter than the DT moderately absorbing aerosol model of 0.008 when AOD is high. In the cluster analysis, we also found that the real part of the refractive index showed no discernable variation with the AOD or wavelength. As such, an average value of 1.53 was assumed for the real part of the refractive index. This particular average value is only derived for the domain of interest (DOI) and determined primarily for biomass burning smoke conditions. Corresponding to Fig. S3, which shows SSA, Figure S4 shows the imaginary part of the refractive index, which mainly controls the absorptivity of the aerosol; it decreases as AOD increases, indicating that a more scattering aerosol would present when AOD is high.

4. Retrieval demonstration and validation

The retrieval algorithm was applied to two cases over the western U.S. during the fire seasons of 2017 and 2020. The first case was from Sept. 4th to 10th, 2017, when multiple fires occurred in northern California, Oregon, and Idaho simultaneously. Figure 3 shows the DOI of the first case, where AERONET had 11 sites with daytime measurements and 3 sites with nighttime measurements during the first case study. We compared the VIIRS nighttime AOD (τ_{DNB}) retrieved in the work with AERONET τ_{AID} and CALIOP nighttime AOD (τ_{CN}). MERRA-2 nighttime AOD interpolated for the VIIRS overpass time (τ_{M2}) was also included in the comparison. The second case was from Sept. 25th to Oct. 6th, 2020. In the second case, the DOI

was extended by 5 degrees to the east to include a special event of local smoke transport that occurred in Colorado; this event showed a distinct diurnal variation pattern that can highlight the importance of this work. Within the DOI for case II, AERONET had 24 sites with daytime measurements and 12 sites with nighttime measurements available. It should be noted that the spatial comparison of τ_{CN} and τ_{DNB} is presented and discussed in case I. For case II, this comparison can be found in the supplemental materials (Figure S6).

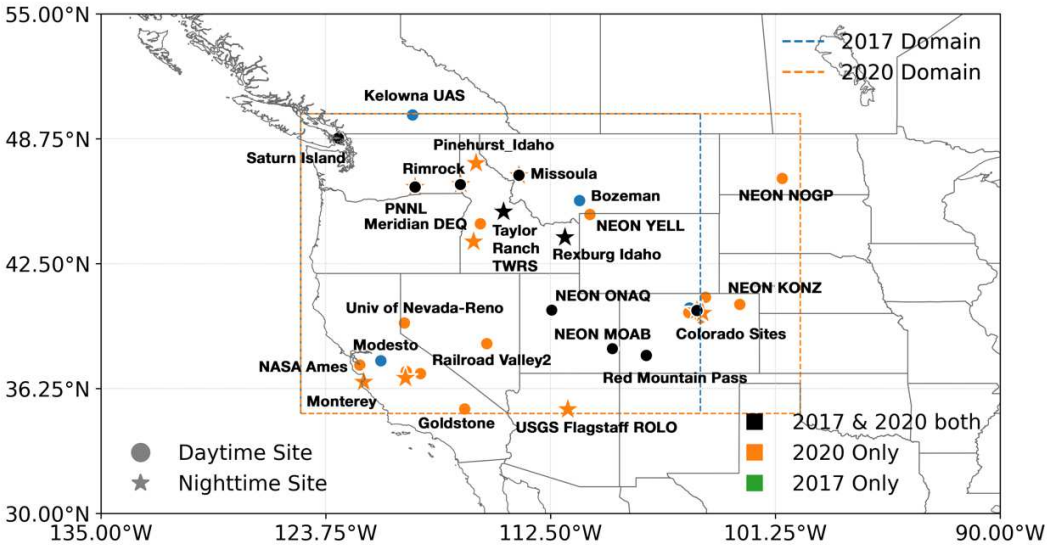

Figure 3. DOI of the case studies. The dashed line denotes the DOI. The black dots represent the locations of the daytime AERONET sites, and the stars represent the nighttime sites.

4.1. 2017 fire season

Figure 4 shows the nighttime DNB image and daytime true color images of the two selected days (Sept. 6th and Sept. 7th, 2017) in the first case study over the DOI. Fires are marked as red dots in the figure. Hundreds of fire events occurred within the DOI, including the Oak Fire in Northern California, the Chetco Bar Fire in Southern Oregon, the Highline Fire in Idaho, and the Conrow Fire in Montana (Fig. 4b and 4d). These persistent fires produced copious smoke that significantly

degraded the regional air quality. As shown in the synoptic map in Figure S5, a high-pressure system in the Northwest and a low-pressure system in the Quebec region caused strong eastward smoke transport that went through the Cascades and Rockies and reached as far east as the Great Lakes region. These fresh smoke episodes scattered more moonlight back to space than the more typical pristine conditions and can even be discerned in the nighttime images as shown in Fig. 4a and 4c. Indeed, the moon illumination factors (MIF) during the period of Sept. 4th to 10th increased from 86% to 100%, then decreased to 73%, providing good MIF conditions for the aerosol retrieval.

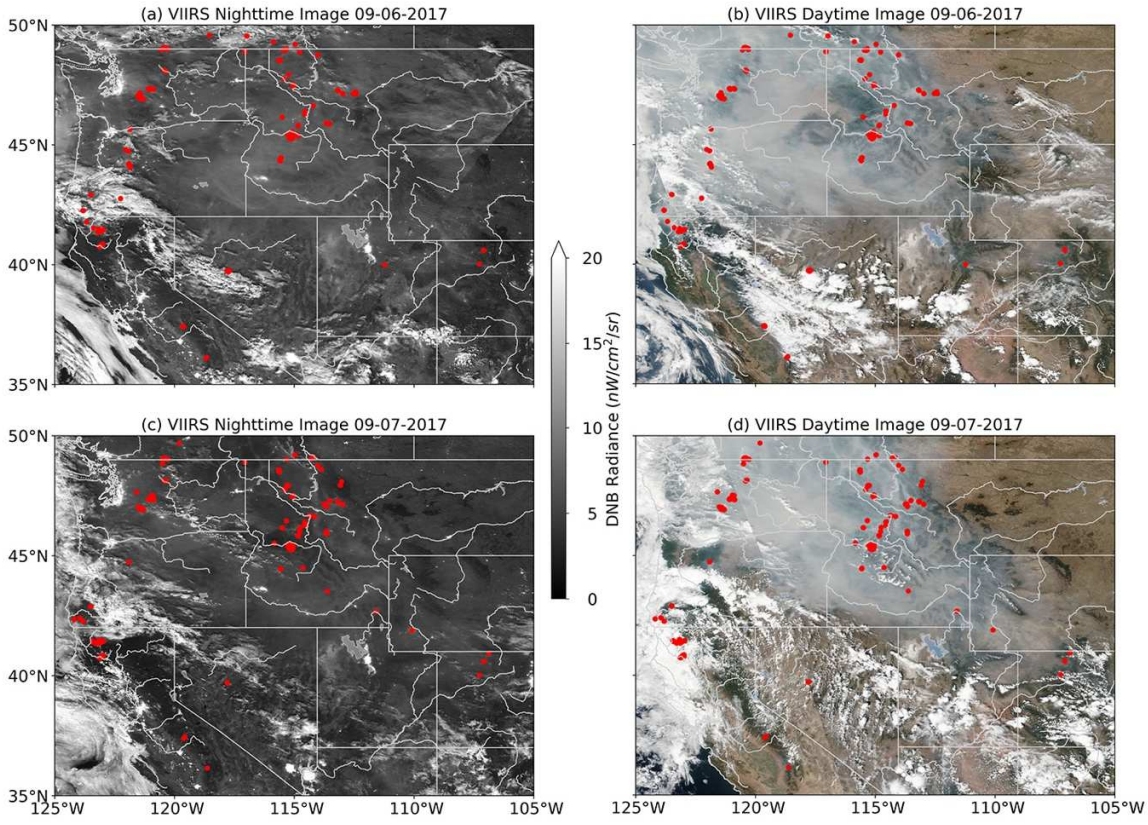

Figure 4. VIIRS nighttime DNB images (left column) and daytime true color images for the selected two consecutive days. (a) 10:30 UTC, Sept. 6th, 2017; (b) 20:20 UTC, Sept. 6th, 2017; (c) 10:12 UTC, Sept. 7th, 2017; (d) 19:48 UTC, Sept. 7th, 2017. The red dots on the map represent the

553 fire pixels adopted from the VIIRS operational activate fire detection algorithm (VNP14). See text
554 for details.
555
556 The spatial distribution of nighttime AOD retrieved over rural regions in the DOI from VIIRS
557 DNB, and its comparison with the MODIS MAIAC AOD in daytime, are shown in Figure 5 (local
558 time is ~ 6 - 7 hours behind UTC). In general, the DNB-derived AODs show good spatial
559 agreement and temporal continuation with the daytime MODIS MAIAC counterparts. The
560 nighttime AOD values are also comparable to those of MAIAC, and together they provide a more
561 complete description of the temporal progression of smoke transport than either of them alone. As
562 shown in Fig. 5, a very dense smoke layer drifted from the U.S. northwest coastline to the U.S.
563 inter-mountain west and high plains area. In the early morning on Sept. 6th (nighttime), the smoke
564 reached mid-Idaho, while southeast Idaho remained clean as shown in Fig. 5a. After 10 hours of
565 daytime transport, smoke layers covered the entire state of Idaho, as shown in Fig. 5b. However,
566 this smoke layer barely progressed eastward for the next 10 hours, as evident when comparing the
567 daytime and nighttime AOD maps of Fig. 5b and Fig. 5c. Over the following 8 hours, the smoke
568 gradually moved eastward and finally entered western Wyoming, as shown in the daytime AOD
569 in Fig. 5d. Also, high AOD values can be observed over Seattle in both DNB AOD and MODIS
570 MAIAC AOD, while on the borders between Washington, Oregon, and Idaho, both retrievals show
571 relatively low AOD on Sept. 6th when compared to surrounding areas. It can also be observed that
572 the low AOD layer moved eastward from 0230 local time (Fig. 5a) to 1300 local time (Fig. 5b). It
573 is apparent that the map of nighttime AOD distribution supplements the daytime AOD map to
574 offer a more insightful and complete description of diurnal smoke transport, which is highly
575 nonlinear. The AOD map at night cannot be obtained by simply interpolating the two daytime

576 AOD maps because (a) the transport is not linear as a function of time, and (2) new smoke layers
577 can be generated by new fires at night.

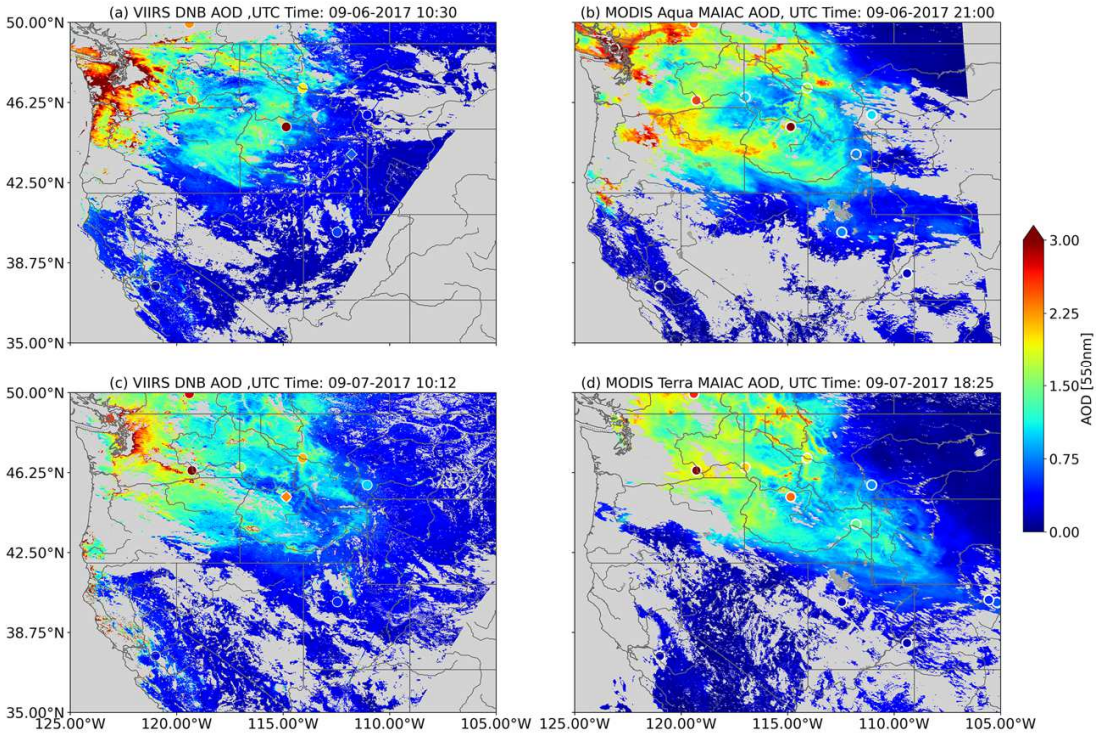

578

579 Figure 5. Comparison of the DNB-retrieved AOD and MODIS MAIAC AOD. (a) DNB AOD at
580 1030 UTC, Sept. 6th, 2017; (b) MODIS MAIAC AOD at 2100 UTC, Sept. 6th, 2017; (c) DNB
581 AOD at 1012 UTC, Sept. 7th, 2017; (d) MODIS MAIAC AOD at UTC 18:25, Sept. 7th, 2017. The
582 circles denote the AERONET daytime AOD measurements, while the diamonds denote the
583 AERONET nighttime AOD measurements. See text for details.

584

585 Furthermore, because atmospheric conditions are often relatively stable at night, the presence of
586 the cloud at night would be less frequent than in the daytime (Bergman & Salby, 1997; Delgado-
587 Bonal et al., 2020). Thus, it is possible to have more AOD retrieval during the night. Figure 6
588 compares the AOD retrieval frequency coverage of the DNB and MODIS MAIAC during the

589 seven days of the first case study. It is clear that, for the western coastal states of California and
590 Oregon, the nighttime AOD maps have higher spatial and temporal coverages, often offering valid
591 AOD values for 5~6 days out of 7 for a given location. For daytime Terra and Aqua, the valid
592 sampling rate is 3~4 days out of 7. For daytime cloud-prone regions near the west coastline,
593 MODIS Aqua has only 1~2 days with AOD reported during one week's time; however, that
594 number is up to 5 days for VIIRS nighttime AOD. In general, the average daily retrieval rate of
595 DNB is ~80%, which is much higher than ~58% of the MODIS MAIAC. Of course, the
596 comparison results could be different on moonless nights when our technique cannot be applied.
597 It is possible that the bright surface could also cause AOD retrieval for algorithms such as MODIS
598 dark target to be missed. However, for MODIS MAIAC, this impact could be small since it utilized
599 the blue band, where the impact of surface reflectance is small, to retrieve AOD. Therefore, the
600 bright surface should have little impact on the retrieval ability of MODIS MAIAC AOD, and the
601 comparison was aimed to investigate the impact of diurnal cloud variation on AOD retrieval
602 ability.

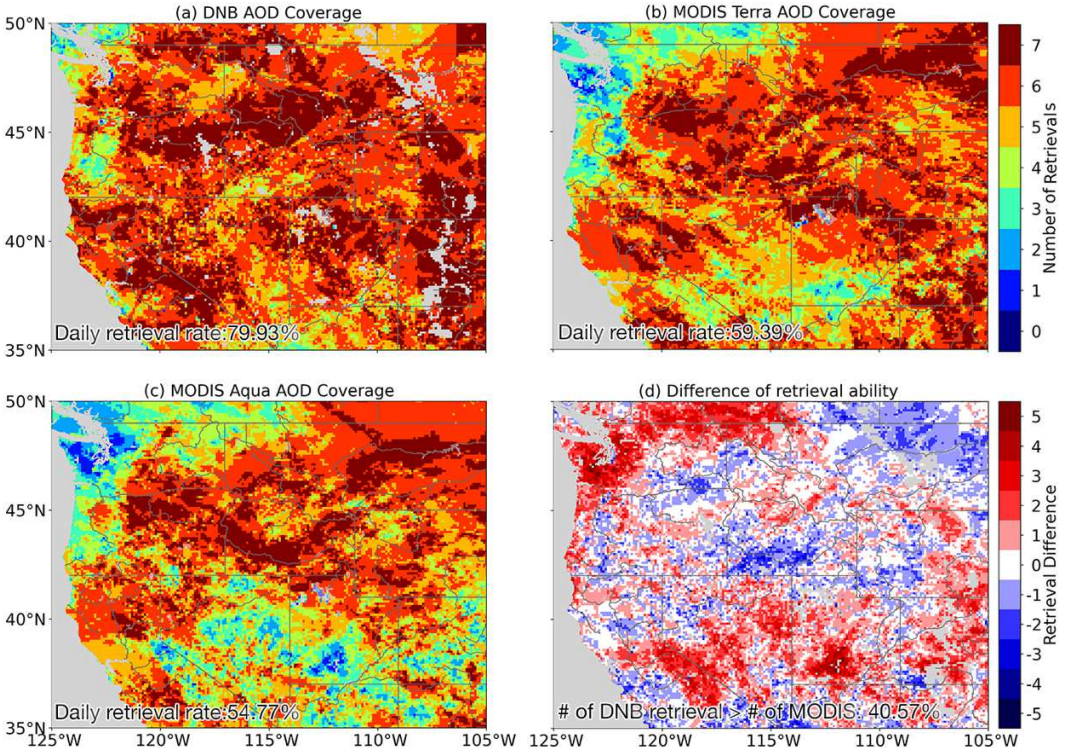

603

604 Figure 6. Spatial distribution of number of days having AOD retrievals from (a) the VIIRS DNB
605 nighttime retrieval algorithm, (b) MODIS Terra daytime retrieval, and (c) MODIS Aqua daytime
606 retrieval, on 7 days from Sept. 04th to 10th, 2017. (d) Difference of the (a) and the average of (b)
607 and (c). The AOD is aggregated to 0.1 × 0.1 degree.

608

609 Figure 7 shows the quantitative comparison of the τ_{DNB} with τ_{AID} and τ_{CN}. Also shown is the
610 comparison with τ_{M2}. Clearly, τ_{DNB} is better correlated with τ_{AID} with a correlation coefficient
611 (R) of 0.94 comparing to τ_{M2} and τ_{AID} pairs (R = 0.79). The root mean square error (RMSE) of
612 τ_{DNB} is 0.15, much lower than the 0.3 of MERRA-2. The total amount of data points in τ_{DNB} is
613 less than that of MERRA-2 because τ_{DNB} is retrieved in cloud-free (clear-sky) conditions only.
614 Although data samplings were limited, the collocated AERONET-DNB AOD pairs show 62.5%
615 falling in an uncertainty envelope of ±(0.085+0.10AOD). However, the DNB AOD shows a

positive bias of ~0.03, indicating that our work tends to overestimate the AOD compared to the AERONET counterpart. This overestimation may be caused by the artificial light contamination surrounding the AERONET sites, although city light pixels are masked before retrieval. The path radiance from the cities and other transient and semi-transient surface light sources, such as traffic lights and wildfires, would illuminate the pixels surrounding the AERONET sites, thus increasing the TOA reflectance and consequently leading to a positive bias of τ_{DNB} retrievals. This bias is expected to be larger when the aerosol loading is larger and the multiple scatterings of atmosphere are enhanced, leading to larger path radiance at the location near the light source. This 3D effect is not considered in our retrieval.

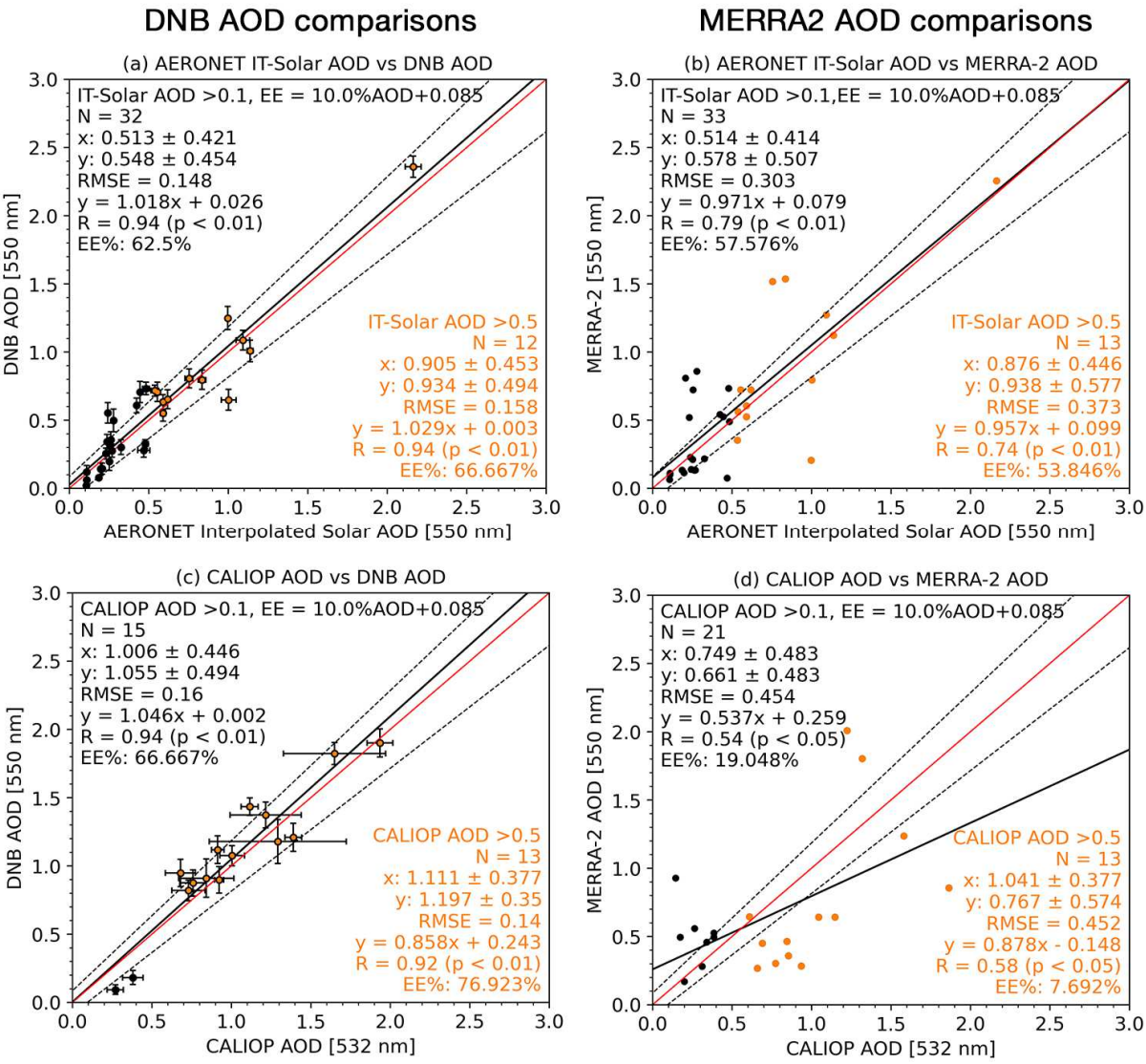

Figure 7. Inter-comparison of the nighttime VIIRS DNB AOD and MERRA-2 AOD on Sept. 4th, 2017, with AEROENET and CALIOP AOD. (a) DNB AOD and (b) MERRA-2 vs. AERONET interpolated AOD from daytime observations. (c) DNB AOD and (d) MERRA-2 vs. CALIOP AOD. The solid red line is the 1:1 line, the solid black line is the regression line, and the dotted lines represent the AOD error envelopes (EE) ± (0.085+0.1AOD). The orange dots denote AODs that are greater than 0.5 (e.g., smoke conditions). See text for details.

In reference to τ_{CN}, τ_{DNB} shows better performance in describing the spatial variation of smoke at night than τ_{M2} (Fig. 7c-d). On Sept. 4th, CALIPSO overpassed the DOI. Figure 8 shows the map of the τ_{DNB} and CALIOP backscattering image. Wildfires are marked as red dots in Fig. 8a. Driven by a high-pressure system presenting in southeastern Oregon, the smoke plumes generated by the wildfires were transported to the north and then to the east, covering Washington, Idaho, and Montana. τ_{CN} was aggregated to 50 km and denoted as color dots along with the CALIOP ground trajectory in Fig. 8b. Fig. 8c is the CALIOP backscattering image. τ_{CN} and τ_{DNB} are denoted as white and orange lines in the images. As shown in Fig. 8b and 8c, the DNB retrieval captures the elevated AOD that CALIOP observed in the areas between 46.25°N, -117.39°W and 42.5°N, -120.19°W. Indeed, the CALIOP AOD reached its peak of ~2 at 48.2°N, 118.2° W, an area downwind from the fires that originated at the edge of Washington and British Columbia. Unfortunately, the DNB approach provides few retrievals over these regions due to significant cloud cover, as verified by the backscattering image in Figure 9c. In areas that were gradually far away from the fire source region, the spatial variation of τ_{DNB} matched well with that of τ_{CN}, especially for areas in the middle of Oregon. As a contrast, although MERRA-2 does provide full spatial coverage of AOD, it missed the AOD peak around 48.2°N, 118.2°W and misplaced the AOD peak around 45.34°N, 119.2°W. We point out that MERRA-2 does not assimilate aerosol height information from CALIOP, so its assumptions that smoke emissions occur in the boundary layer could explain the incorrect transport where, for this event, the smoke is seen in an elevated layer (Fig. 8c).

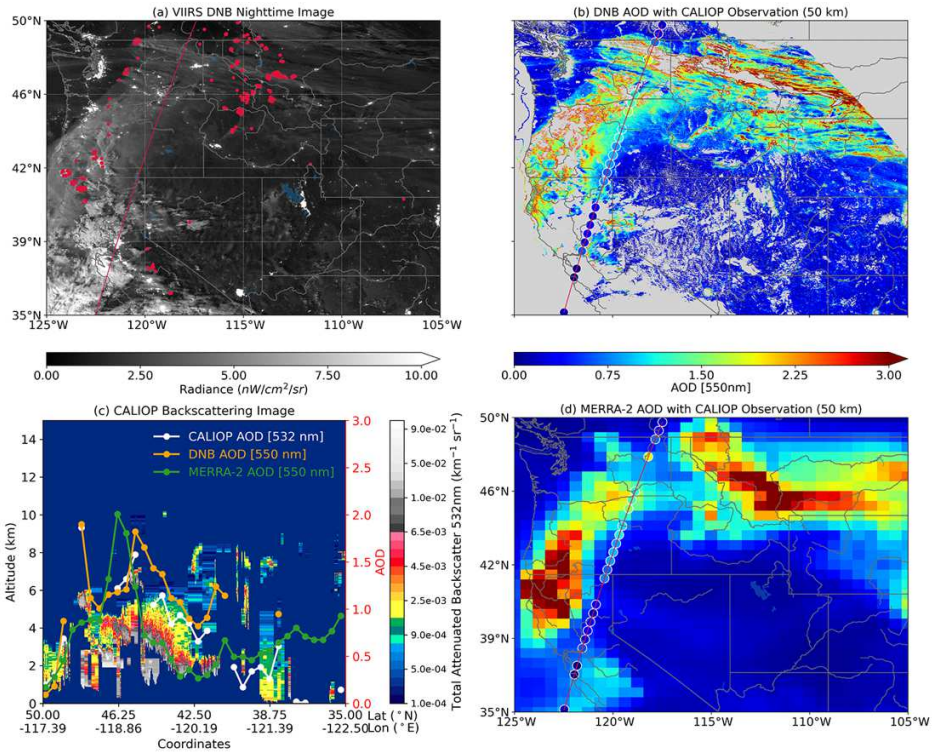

653

654 Figure 8. Inter-comparison DNB AOD retrieval with CALIOP observations on Sept. 4th, 2017. (a)
655 VIIRS nighttime image, (b) DNB AOD map with CALIOP observations, (c) CALIOP
656 backscattering image overlaid with AOD (right y-axis) retrieved from VIIRS DNB, MERRA-2,
657 and CALIOP, (d) MERRA-2 AOD map with CALIOP AOD. The white line in (c) is the CALIOP
658 AOD trajectory, while the orange and green lines are the AOD trajectories of VIIRS DNB and
659 MERRA-2, respectively.

660

661 The quantitative comparison between τ_{DNB} and τ_{CN} is shown in Fig. 7c. In general, τ_{DNB}
662 correlated positively with τ_{CN} with R of 0.94 and RMSE of 0.16, and 67% of the τ_{DNB}-τ_{CN} pairs
663 fell in the uncertainty envelope. For most of the paired data (~70%), τ_{DNB} values slightly
664 overestimate τ_{CN} value, especially at elevated smoke regions in between 46.25° N, -117.39° W
665 and 42.5° N, -120.19° W. This bias may be caused by a complicated mix of cloud and aerosol over

666 that region, as shown in Fig. 8c. While CALIOP can distinguish the particle type, DNB only
667 reveals the column total optical depth. However, DNB does provide AOD retrieval over large
668 areas, providing quantitative information on long-range smoke transport at night.
669
670 *4.2. 2020 fire season*
671 The second case study took place during the 2020 fire season, from Sept. 28th to Nov. 5th, when
672 the lunar illuminance factor increased from 90% to 100% and then dropped to 90%. Figure 9 shows
673 the satellite images (left column) and the corresponding map of AOD retrievals (right column).
674 Red dots on the satellite images denote the fire spots detected by the VIIRS active fire detection
675 algorithm. Fig. 9a and 9c are the true-color images of Sept. 29th and 30th, while Fig. 9e and 9g
676 show the corresponding daytime AOD retrieved by the MODIS MAIAC algorithm from Terra and
677 Aqua observation, respectively. These results indicate that smoke generated by the persistent
678 wildfire in coastal California was transported by synoptic scale flow patterns to the southeast.
679 However, upon arrival in the Rocky Mountain region (e.g., Wyoming, Colorado, and New Mexico)
680 the spatial distribution of smoke showed two distinguishable patterns, revealed in the map of the
681 consecutive daytime AOD retrievals in Fig. 9e and Fig. 9g, respectively. In the early afternoon of
682 Sept. 29th, the smoke generated by the fires that happened in the southern part of Wyoming showed
683 a southeastern transport under the influence of the westerly wind as indicated in Fig. 9e. However,
684 around noon on Sept. 30th, the AOD map of Fig. 9g generated by MODIS shows a vast dispersion
685 of smoke over eastern Colorado and northern New Mexico. Several striped shapes of smoke
686 transport can be clearly discerned in Fig. 9g. When only daytime observations are included in the
687 analysis, it is difficult to interpret the sudden pattern change of the smoke transport over this region;
688 the nighttime information provides important additional context.

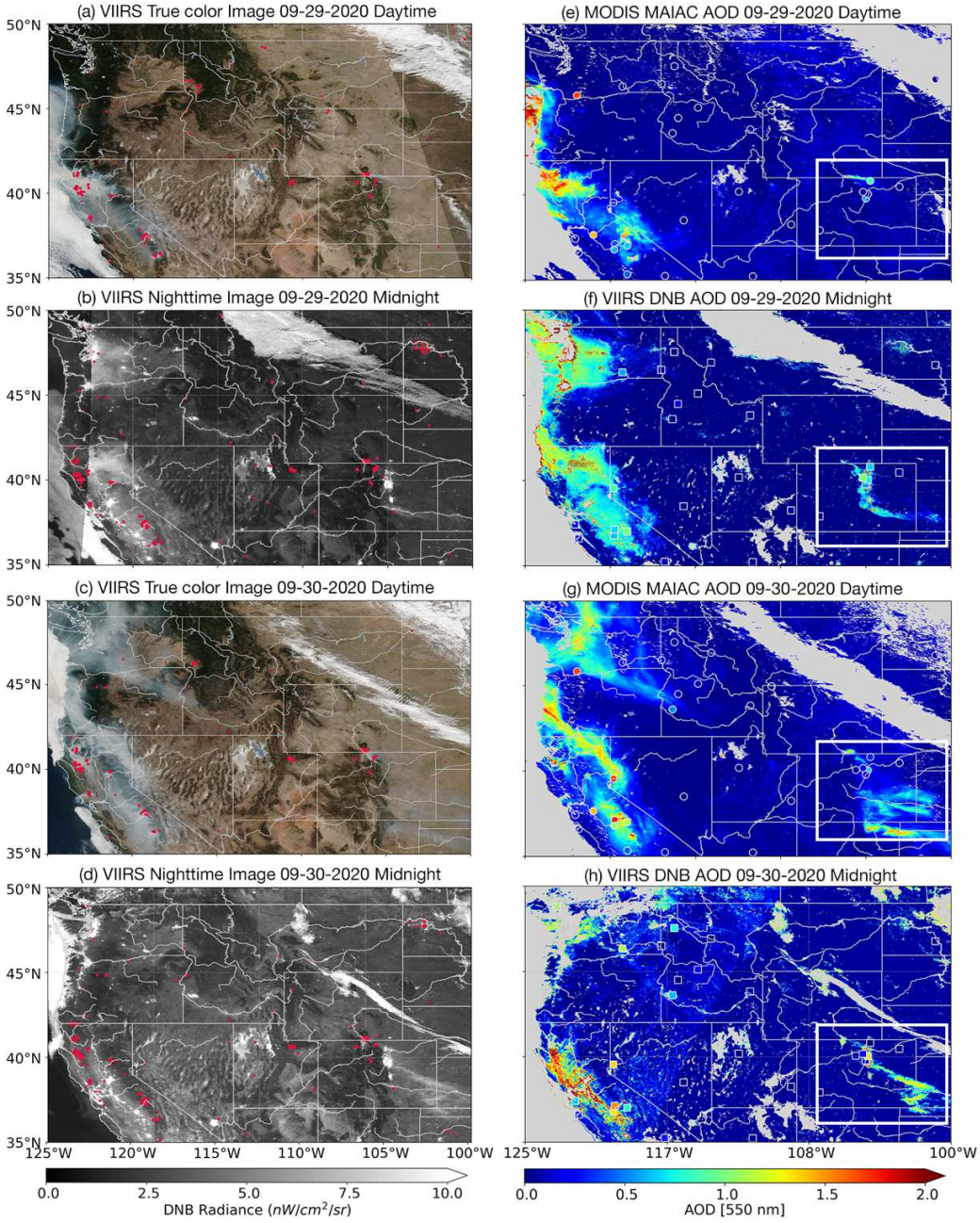

Figure 9. Satellite images and AOD retrievals for case II. (a - b): VIIRS NPP true color and nighttime DNB image on Sept. 29th, 2020. (c - d) are the same as (a - b), but for Sept. 30th, 2020. (e-h) AOD retrievals for the corresponding satellite observations from MODIS and VIIRS DNB in the left column. The white boxes in the AOD map indicate the domain of the special smoke transport events that occurred over the Colorado region. The circles denote the AERONET

695 daytime AOD measurements, while the diamonds denote the AERONET nighttime AOD
696 measurements.
697
698 Fig. 9f presents the nighttime AOD retrieved in this work. When Fig. 9f and its daytime counterpart
699 (Fig. 9g) are compared, there is general agreement of the spatial distribution and magnitude of the
700 AOD between the MODIS MAIAC and nighttime DNB retrievals. However, there are some
701 discrepancies over a small area in California, where the DNB AOD reaches 2 while the daytime
702 AOD is around 1.0~1.5. One possible explanation of the overestimation (if we treat the daytime
703 AOD as truth) could be sub-pixel low stratus contamination. As mentioned earlier, the current
704 retrieval algorithm relied mainly on the TIR band to separate the cloud from the cloud-free
705 background, but the TIR technique may be subject to misclassifying low stratus clouds as aerosol
706 layers. Further refinement of cloud mask is planned for future studies.
707
708 More interesting day-night differences were discerned over the Midwest, indicating that the diurnal
709 variation of the smoke transport is nonlinear. First, the smoke was primarily transported to the east
710 over the Washington region as shown in Fig. 9f, while the following morning, MODIS AOD
711 indicated a southeasterly dominant transport to the southwest. Second, DNB AOD retrievals
712 indicate that the smoke over the Rocky Mountain region was transported southward along the
713 Front Range of the Rockies, forming an “L” shape in the AOD distribution that cannot be seen
714 from the daytime AOD observations.
715
716 Figure 10a offers a close-in view of the AOD map for the special events over the Colorado region
717 presented in Fig. 9. MERRA-2 AOD data were used as a comparison, as shown in Fig. 10b. The

meteorological fields from the NCEP's High Resolution Rapid Refresh (HRRR) (Blaylock et al., 2017) model (3 km spatial resolution) were used to help interpret the observed L shape of AOD distribution. As shown in Fig. 10a and the vertical wind structure of Fig. 10c, the wind direction at 750 mb and higher pressure levels was dominated by a northerly wind, indicating that the meteorological conditions at the Front Range of the Rocky Mountain (denoted as the second segment in both figures) favor the transport of smoke to the south. After reaching Pueblo, the smoke was transported along the Arkansas River, forming the other limb of the L shape shown as Segment 3. This sudden change of transport direction can be rationalized by examining the third segment of the wind distribution in Fig. 10c. A weak eastward wind dominates between the surface and the pressure level of 750 mb and below. This sudden change in wind direction may be a result of combined effects of meteorology and topography that finally favored the eastern transport of smoke. This nighttime L shape of smoke distribution can also partially explain several strips of AOD that presented over eastern Colorado around noon the following day. During the daytime of Sept. 30th, with the increase of the zonal wind speed, the wind carried the smoke that was at the Front Range of the Rocky Mountains the previous night to Eastern Colorado. This event also emphasizes the importance of having nighttime retrieval of AOD. Traditionally, a linear interpolation of the two daytime AOD maps would be used to create the nighttime map of AOD. In this highly nonlinear-with-time transport case, the linear interpolation of daytime-retrieved AOD would overemphasize the AOD over western Colorado, which is not present in the observed nighttime AOD by VIIRS, and the sharp southerly feature would be missed entirely.

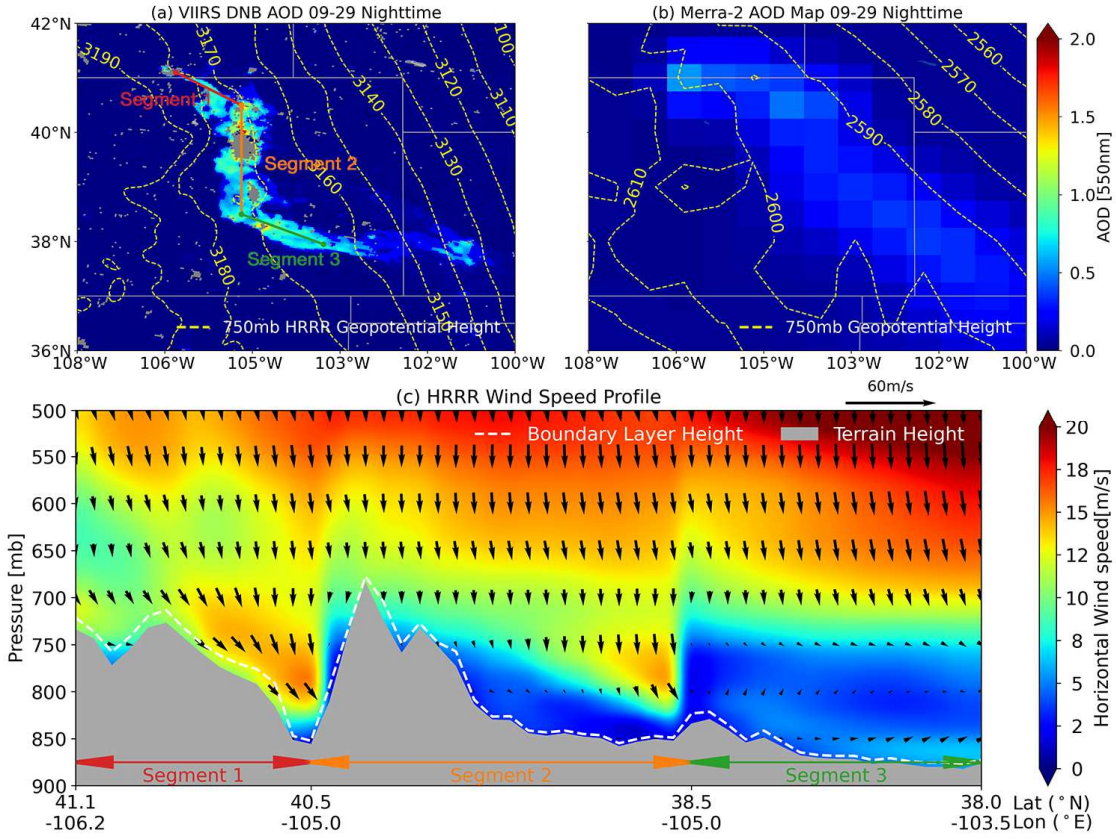

739

740 Figure 10. Zoomed-in plot of the AOD map over the Colorado region. (a) DNB AOD map at
741 midnight of Sept. 29th, 2020; (b) MERRA-2 AOD map at VIIRS overpass time; (c) HRRR wind
742 profile at VIIRS overpass time. The yellow dashed line on the DNB AOD map is the 750 mb
743 geopotential height (in unit of m) contour extracted from HRRR, while the yellow dashed line on
744 the MERRA-2 map is the 750 mb geopotential height contour of MERRA-2. The L-shaped
745 distribution of smoke layer in (a) is marked with three colored lines denoting three segments. Also
746 shown is the horizonal wind vector in (c) at different pressure levels, with north pointing upward.
747 Note that a small but eastward (pointing to the right-hand side) dominated wind was found in
748 Segment 3 at and below the 750 mb pressure level, favoring the formation of the L shape of the
749 AOD map.

750

751 Quantitative comparisons of τ_{DNB} with multiple sources of AOD are shown in Figure 11. Similar
752 to case I, τ_{M2} is used as a reference for comparison. The significant difference in the data points
753 available for τ_{AID} and the lunar AODs (τ_{LNR}) are due to the fact that τ_{AID} relies on a 20-hour
754 temporal window to acquire two data points from the AERONET daytime measurements, which
755 may be rather difficult compared to direct nighttime measurements. Fig. 11 shows that comparison
756 results corroborate the conclusions drawn from the first case studies; τ_{DNB} correlates with τ_{AID},
757 τ_{CN}, and τ_{LNR} with R values of 0.89, 0.96, and 0.95, respectively. The corresponding RMSEs are
758 0.22, 0.17, and 0.15, respectively. Further error analysis toward the comparison of τ_{LNR} and τ_{DNB}
759 indicates that the 1σ retrieval error are ~0.086. For MERRA-2, the statistics comparison of τ_{M2}
760 and the three AOD datasets (τ_{AID}, τ_{CN}, and τ_{LNR}) indicates that the model performance at night is
761 not as good as daytime performance when several observed AOD datasets are assimilated. When
762 AOD is greater than 0.5, the statistics are even worse. For example, only 44% of the $\tau_{\mathrm{M2}} -$
763 τ_{LNR} pairs fall into the defined error envelopes, compared to 72% of the $\tau_{\mathrm{DNB}} - \tau_{\mathrm{LNR}}$ pairs. This
764 indicates that a pure nighttime AOD is important to constrain the model simulation for high AOD
765 scenarios like smoke events at night. However, for Fig. 11a, only 52% of the τ_{DNB} and τ_{AID} pairs
766 fall in the uncertainty envelopes. The fractions increase to 86% and 69% for the τ_{DNB} and τ_{CN}
767 pairs and τ_{DNB} and τ_{LNR} pairs, shown as Fig. 11c and Fig. 11e. This again indicates that although
768 interpolating daytime AOD to nighttime is a convenient way of getting references for nighttime
769 AOD, it may introduce errors and cannot explain the nonlinear diurnal variation of the AOD.
770

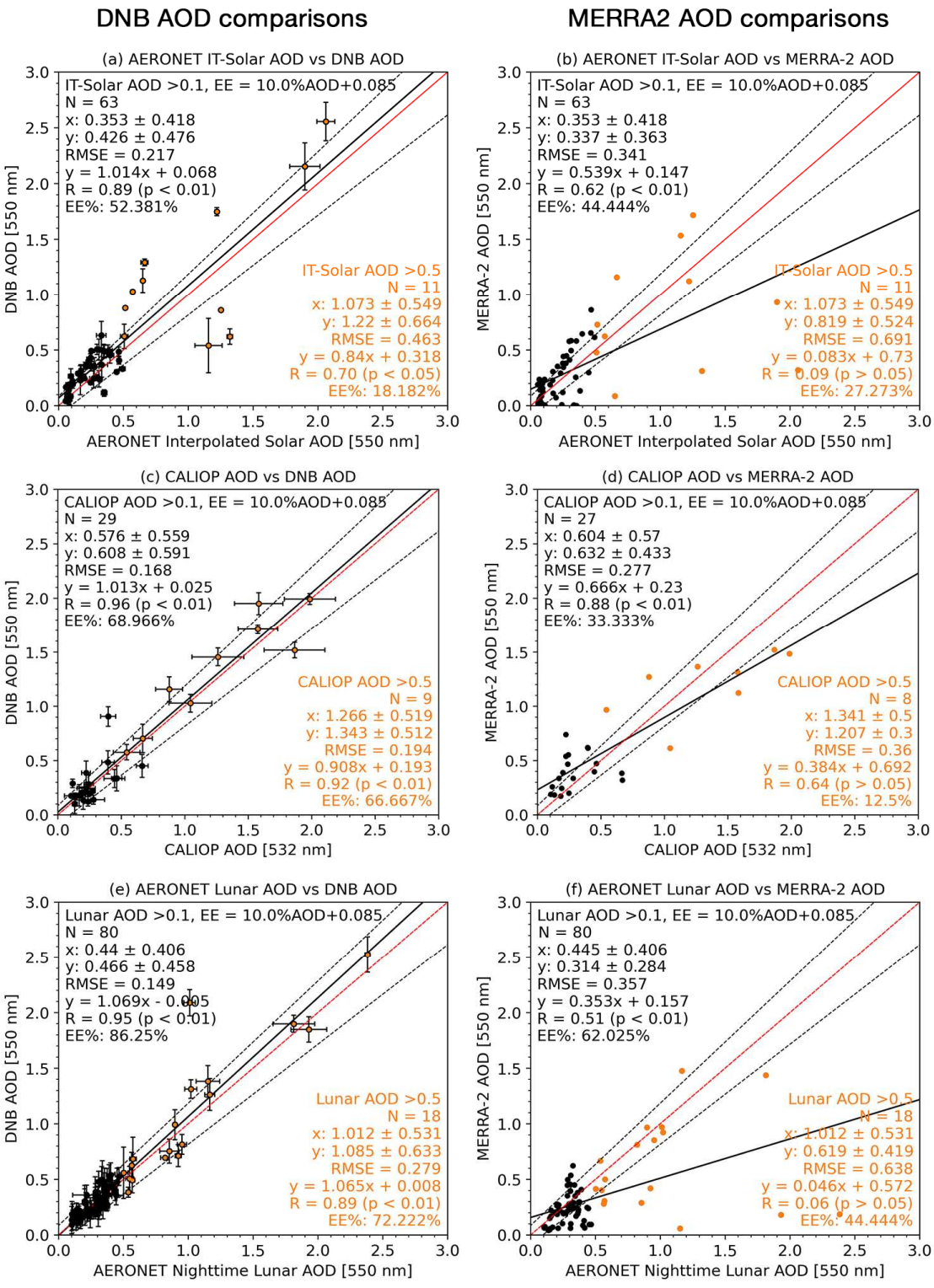
DNB AOD comparisons
MERRA2 AOD comparisons
(a) AERONET IT-Solar AOD vs DNB AOD
IT-Solar AOD >0.1, EE = 10.0%AOD+0.085
N = 63
x: 0.353 ± 0.418
y: 0.426 ± 0.476
RMSE = 0.217
y = 1.014x + 0.068
R = 0.89 (p < 0.01)
EE%: 52.381%
IT-Solar AOD >0.5
N = 11
x: 1.073 ± 0.549
y: 1.22 ± 0.664
RMSE = 0.463
y = 0.84x + 0.318
R = 0.70 (p < 0.05)
EE%: 18.182%
DNB AOD [550 nm]
AERONET Interpolated Solar AOD [550 nm]
(b) AERONET IT-Solar AOD vs MERRA-2 AOD
IT-Solar AOD >0.1, EE = 10.0%AOD+0.085
N = 63
x: 0.353 ± 0.418
y: 0.337 ± 0.363
RMSE = 0.341
y = 0.539x + 0.147
R = 0.62 (p < 0.01)
EE%: 44.444%
IT-Solar AOD >0.5
N = 11
x: 1.073 ± 0.549
y: 0.819 ± 0.524
RMSE = 0.691
y = 0.083x + 0.73
R = 0.09 (p > 0.05)
EE%: 27.273%
MERRA-2 AOD [550 nm]
AERONET Interpolated Solar AOD [550 nm]
(c) CALIOP AOD vs DNB AOD
CALIOP AOD >0.1, EE = 10.0%AOD+0.085
N = 29
x: 0.576 ± 0.559
y: 0.608 ± 0.591
RMSE = 0.168
y = 1.013x + 0.025
R = 0.96 (p < 0.01)
EE%: 68.966%
CALIOP AOD >0.5
N = 9
x: 1.266 ± 0.519
y: 1.343 ± 0.512
RMSE = 0.194
y = 0.908x + 0.193
R = 0.92 (p < 0.01)
EE%: 66.667%
DNB AOD [550 nm]
CALIOP AOD [532 nm]
(d) CALIOP AOD vs MERRA-2 AOD
CALIOP AOD >0.1, EE = 10.0%AOD+0.085
N = 27
x: 0.604 ± 0.57
y: 0.632 ± 0.433
RMSE = 0.277
y = 0.666x + 0.23
R = 0.88 (p < 0.01)
EE%: 33.333%
CALIOP AOD >0.5
N = 8
x: 1.341 ± 0.5
y: 1.207 ± 0.3
RMSE = 0.36
y = 0.384x + 0.692
R = 0.64 (p > 0.05)
EE%: 12.5%
MERRA-2 AOD [550 nm]
CALIOP AOD [532 nm]
(e) AERONET Lunar AOD vs DNB AOD
Lunar AOD >0.1, EE = 10.0%AOD+0.085
N = 80
x: 0.44 ± 0.406
y: 0.466 ± 0.458
RMSE = 0.149
y = 1.069x - 0.005
R = 0.95 (p < 0.01)
EE%: 86.25%
Lunar AOD >0.5
N = 18
x: 1.012 ± 0.531
y: 1.085 ± 0.633
RMSE = 0.279
y = 1.065x + 0.008
R = 0.89 (p < 0.01)
EE%: 72.222%
DNB AOD [550 nm]
AERONET Nighttime Lunar AOD [550 nm]
(f) AERONET Lunar AOD vs MERRA-2 AOD
Lunar AOD >0.1, EE = 10.0%AOD+0.085
N = 80
x: 0.445 ± 0.406
y: 0.314 ± 0.284
RMSE = 0.357
y = 0.353x + 0.157
R = 0.51 (p < 0.01)
EE%: 62.025%
Lunar AOD >0.5
N = 18
x: 1.012 ± 0.531
y: 0.619 ± 0.419
RMSE = 0.638
y = 0.046x + 0.572
R = 0.06 (p > 0.05)
EE%: 44.444%
MERRA-2 AOD [550 nm]
AERONET Nighttime Lunar AOD [550 nm]

771

772 Figure 11. Inter-comparison of the retrieved and model AOD with observations for the study case
773 in the 2020 fire season. (a) DNB AOD vs. AERONET interpolated AOD. (b) MERRA-2 vs.
774 AERONET interpolated AOD for Sept. 28th to Oct. 5th, 2020. (c) DNB AOD vs. CALIOP AOD.
775 (d) MERRA-2 vs. CALIOP AOD for Oct. 1st and 3rd, 2020. (e) DNB AOD vs. AERONET
776 nighttime lunar AOD. (f) MERRA-2 AOD vs. AERONET nighttime lunar AOD. The dotted lines
777 represent the AOD error envelopes ±(0.085+10% AOD). The orange dots denote AODs that are
778 greater than 0.5. See text for details.
779
780 *4.3. Uncertainty Analysis*
781 The uncertainty sources of τ_{DNB} essentially lie in four areas: (1) the lunar irradiance database, (2)
782 the DNB calibration uncertainty, (3) the surface representation, and (4) the aerosol models. While
783 the lunar irradiance database and DNB calibration are independent uncertainty sources for the
784 DNB retrieval, they function together to determine the TOA reflectance of the DNB observation.
785 Miller and Turner (2009) estimated that the overall uncertainty of the lunar irradiance database is
786 7% ~ 17%, increasing with the moon phase angle. For most of the scenarios that DNB can observe,
787 this uncertainty is 7% ~ 12%. Because the dynamic range of the DNB observation is in
788 approximately seven orders of magnitude for its corresponding low/mid/high gain stage, the
789 radiometric calibration of the DNB is complex (Chen et al., 2017; Lei et al., 2020). For the
790 nighttime scenarios where the high gain stage is applied, calibration uncertainty is approximately
791 15% across the entire radiometric range. To evaluate the effect of the TOA reflectance on the
792 retrieval, we changed the lunar irradiance by ±12% and ±15% while keeping the rest of the
793 parameters the same during the retrieval process. Our calculation shows that a 12% change in the
794 TOA reflectance would cause a <17% relative bias of AOD retrieval. For a 15% change, the

795 relative error is <20%. Considering that the monthly AOD at 550 nm is below 0.4 (Li et al., 2015),
796 we estimate the uncertainty due to the lunar irradiance database and DNB calibration will be less
797 than 0.07 and 0.08, respectively.
798
799 The retrieval uncertainty from the surface reflectance characterization is first analyzed by using a
800 long-term analysis of the MODIS surface albedo products. Ten years of MODIS surface albedo
801 products were used to derive the relative deviation (RD) of albedo retrieval at MODIS channel 2
802 (858 nm) and channel 4 (555 nm). We found that the RD was below 1% when the albedo was
803 greater than 0.1 for both channels. The maximum RD occurs when the albedo was extremely small
804 (<0.05) and was less than 7.5%. As shown in Fig. 2(b), a 0.05 error envelope was sufficient to
805 include errors in the RF-based estimates of surface albedo. Thus, a ±(0.05+7.5% albedo) variation
806 of surface albedo was used to test the sensitivity of the surface albedo to the retrievals. However,
807 it should be noted that the 0.05 intercept may lead to a negative albedo when the albedo was smaller
808 than 0.05. In this case, only ±7.5% was applied. The simulation showed that this magnitude of
809 albedo variations would lead to less than 0.03±0.02 AOD uncertainty in AOD retrieval. The
810 uncertainty due to aerosol optical properties has been analyzed in several past studies. Considering
811 an SSA of 0.03 will lead to an AOD retrieval uncertainty of 8% for an AOD around 0.5 (Wang et
812 al., 2003a).
813
814 The uncertainty in AOD retrieval caused by reflectance smoothing using a window of 3×3 pixels
815 was also investigated. The analysis of the spatially and temporally collocated AERONET-VIIRS
816 nighttime AOD pairs (as in Fig. 11) showed that the retrieval error difference was less than 4% as
817 the threshold (number of valid pixels in 3×3 spatial window) for smoothing changed from 5 to 7

and that there was no significant difference as the threshold changed from 7 to 9 (Figure S7). This is expected because if the reflectance of a DNB pixel was missing, it could be an indicator not only that the current pixel had a quality issue, but also that adjacent pixels might contain a certain degree of contamination from, for example, sub-pixel cloud or wildfire.

When dealing with the Rayleigh scattering, the current algorithm adopted a fixed mid-latitude summer atmospheric profile with surface pressure of 1013 hPa (equivalent to an optical depth of 0.045 after consideration of the DNB spectral range and relative response functions), which may introduce a 0.01 low bias into the AOD retrieval (since in most place, surface pressure over land varies less than 20% from 1013 hPa).

Through the analysis above, an average uncertainty of 0.12 for the AOD retrieval is expected in this work with a maximum uncertainty of 0.2. Note that those uncertainties from various sources could be random and offset each other. Hence, the overall uncertainty provided here is an upper limit to quantify the total uncertainty of the retrieval. The actual comparison with several independent datasets indicates an average uncertainty (1-sigma) of 0.085 and an uncertainty envelope of 0.085+0.10AOD (in which at least 67% of data pairs reside).

5. Summary and Discussion

We developed the first algorithm for nighttime aerosol optical depth retrieval from VIIRS DNB moonlight observation. The algorithm was applied to DNB observations for wildfire events over the continental U.S. for Sept. 2017 and Oct. 2020, when large amounts of smoke were generated by the persistent wildfires and transported across the continental U.S. We found that the AOD

841 values retrieved from DNB were in good agreement with the AOD retrieved from multiple sources
842 such as MODIS MAIAC, CALIOP, and AERONET. For both smoke events illustrated in this
843 paper, the linear correlations are ~0.90, with ~86% of the DNB AOD retrievals falling in a
844 ±(0.085+0.10AOD) uncertainty envelope. The main implications of this work are twofold. First,
845 the DNB nighttime AOD retrievals can provide global aerosol information at night when moon
846 illumination factors (MIF) permits, which allows further study of the diurnal variation of aerosol.
847 Such information is valuable for constraining and evaluating the distribution and concentration of
848 the nighttime aerosols estimated by the chemistry transport model. Second, the retrieved nighttime
849 AOD can be used to provide strong constraints on the forecast of the 24-hour surface air quality.
850 This is clearly illustrated by the fact that the DNB AOD retrieval is superior to the MERRA-2
851 AOD when compared to AERONET, as shown in our case studies.
852
853 Due to the limitations of nighttime observation and the panchromatic property of the DNB sensor,
854 this algorithm is a single-band retrieval and relies on assumptions of surface reflectance and
855 aerosol model. Currently, our algorithm adopts a random forest model to determine the spectral
856 surface reflectance of DNB from MODIS surface climatology. However, the accuracy of the
857 random forest model is limited by the comprehensiveness of the training dataset. Consequently, it
858 may lack the ability to capture the seasonal variation of the surface and may introduce bias to the
859 AOD retrieval. Second, the current algorithm incorporates a wildfire smoke aerosol climatology
860 model derived from AERONET observations during wildfire seasons and thus restricts its
861 application to smoke scenes over the continental U.S. Third, the current algorithm relies on
862 moonlight as its illumination source. Considering the strength of the moonlight and the DNB
863 sensitivity, it will only retrieve AOD for days whose MIF is greater than 75%, which effectively

enables DNB retrieval of 10 days in 30 days. This MIF threshold is slightly higher than that (50%) used in the AERONET nighttime lunar retrieval; the latter enables AERONET to have an average of 15 days with nighttime AOD retrieval in a month. Forth, the moonlight observation may be contaminated by surface light sources such as the light dome effect of city light and the 3D effect of the cloud, or by lights from parts of the active fire itself. Such contamination would introduce a positive bias into the AOD retrieval. Complementary AOD retrieval methods, wherein modulation of known/stable surface lights by intervening aerosol, may be useful in these areas. Nevertheless, the work in this paper further underscores the importance and potential of nighttime AOD remote sensing from space. It is therefore foreseeable that, in the future, a low-light imager with multiple bands could further improve AOD and aerosol properties characterization from space by using moonlight, city light, or both.

Acknowledgments

This study was supported by the NASA FIREX-AQ grant (80NSSC18K0791), the Office of Naval Research (ONR) Multidisciplinary University Research Initiatives (MURI) Program under the award N00014-16-1-2040, and the NASA Terra/Aqua/SNPP Science program. We acknowledge the public availability of VIIRS data from the NASA Earth Observing System Data and Information System (EOSDIS), and the CALIOP Level 2 aerosol profile data from the NASA Langley Research Center Atmospheric Science Data Center. We thank all Principal Investigators, Co-Principal Investigators, and their staff for establishing and maintaining the AERONET sites used in this investigation. We also acknowledge the National Air Pollution Surveillance (NAPS) program of the EPA (https://aqs.epa.gov/aqsweb/airdata/download_files.html) and the

886 NOAA/National Centers for Environmental Prediction (NCEP) for implementing and maintaining
887 HRRR (https://rapidrefresh.noaa.gov/).
888

889 **6. References**

890 Adhikary, B., Kulkarni, S., Dallura, A., Tang, Y., Chai, T., Leung, L. R., et al. (2008). A regional
891 scale chemical transport modeling of Asian aerosols with data assimilation of AOD
892 observations using optimal interpolation technique. *Atmospheric Environment, 42*(37),
893 8600-8615. http://www.sciencedirect.com/science/article/pii/S1352231008007929
894 Anenberg, S. C., Achakulwisut, P., Brauer, M., Moran, D., Apte, J. S., & Henze, D. K. (2019).
895 Particulate matter-attributable mortality and relationships with carbon dioxide in 250
896 urban areas worldwide. *Scientific Reports, 9*(1), 11552. https://doi.org/10.1038/s41598-
897 019-48057-9
898 Barreto, Á., Cuevas, E., Granados-Muñoz, M. J., Alados-Arboledas, L., Romero, P. M., Gröbner,
899 J., et al. (2016). The new sun-sky-lunar Cimel CE318-T multiband photometer – a
900 comprehensive performance evaluation. *Atmos. Meas. Tech., 9*(2), 631-654.
901 https://amt.copernicus.org/articles/9/631/2016/
902 Bergman, J. W., & Salby, M. L. (1997). The Role of Cloud Diurnal Variations in the Time-Mean
903 Energy Budget. Journal of Climate, 10(5), 1114-1124.
904 https://journals.ametsoc.org/view/journals/clim/10/5/1520-
905 0442_1997_010_1114_trocdv_2.0.co_2.xml
906 Berkoff, T. A., Sorokin, M., Stone, T., Eck, T. F., Hoff, R., Welton, E., & Holben, B. (2011).
907 Nocturnal Aerosol Optical Depth Measurements with a Small-Aperture Automated
908 Photometer Using the Moon as a Light Source. *Journal of Atmospheric and Oceanic*

Technology, 28(10), 1297-1306. https://journals.ametsoc.org/view/journals/atot/28/10/jtech-d-10-05036_1.xml

Blaylock, B. K., Horel, J. D., & Liston, S. T. (2017). Cloud archiving and data mining of High-Resolution Rapid Refresh forecast model output. Computers and Geosciences, 109, 43–50. https://doi.org/10.1016/j.cageo.2017.08.005

Boucher, O., Randall, D., Artaxo, P., Bretherton, C., Feingold, G., Forster, P., et al. (2013). Clouds and Aerosols. In T. F. Stocker, D. Qin, G.-K. Plattner, M. Tignor, S. K. Allen, J. Boschung, A. Nauels, Y. Xia, V. Bex, & P. M. Midgley (Eds.), *Climate Change 2013: The Physical Science Basis. Contribution of Working Group I to the Fifth Assessment Report of the Intergovernmental Panel on Climate Change* (pp. 571–658). Cambridge, United Kingdom and New York, NY, USA: Cambridge University Press.

Chen, H., Xiong, X., Sun, C., Chen, X., & Chiang, K. (2017). Suomi-NPP VIIRS day–night band on-orbit calibration and performance. *Journal of applied remote sensing, 11*(3), 036019.

Csiszar, I., Schroeder, W., Giglio, L., Ellicott, E., Vadrevu, K. P., Justice, C. O., & Wind, B. (2014). Active fires from the Suomi NPP Visible Infrared Imaging Radiometer Suite: Product status and first evaluation results. *Journal of Geophysical Research: Atmospheres, 119*(2), 803-816.

Delgado-Bonal, A., Marshak, A., Yang, Y., & Oreopoulos, L. (2020). Daytime variability of cloud fraction from DSCOVR/EPIC observations. Journal of Geophysical Research: Atmospheres, 125(10), e2019JD031488.

Ding, S., Wang, J., & Xu, X. (2016). Polarimetric remote sensing in oxygen A and B bands: sensitivity study and information content analysis for vertical profile of aerosols. *Atmos. Meas. Tech., 9*(5), 2077-2092. https://www.atmos-meas-tech.net/9/2077/2016/

Elvidge, C. D., Baugh, K., Zhizhin, M., Hsu, F. C., & Ghosh, T. (2017). VIIRS night-time lights. *International Journal of Remote Sensing, 38*(21), 5860-5879. https://doi.org/10.1080/01431161.2017.1342050

Fu, D., Xia, X., Duan, M., Zhang, X., Li, X., Wang, J., & Liu, J. (2018). Mapping nighttime PM2.5 from VIIRS DNB using a linear mixed-effect model. *Atmospheric Environment, 178*, 214-222. http://www.sciencedirect.com/science/article/pii/S1352231018300736

Getzewich, B. J., Tackett, J. L., Kar, J., Garnier, A., Vaughan, M. A., & Hunt, B. (2016). CALIOP Calibration: Version 4.0 Algorithm Updates. *EPJ Web of Conferences, 119*, 04013. https://doi.org/10.1051/epjconf/201611904013

Giles, D., Slutsker, I., Schafer, J., Sorokin, M. G., Smirnov, A., Eck, T. F., et al. (2019a). Uncertainty and Bias in AERONET Nighttime AOD Measurements. *AGUFM, 2019*, A23R-3050.

Giles, D. M., Sinyuk, A., Sorokin, M. G., Schafer, J. S., Smirnov, A., Slutsker, I., et al. (2019b). Advancements in the Aerosol Robotic Network (AERONET) Version 3 database–automated near-real-time quality control algorithm with improved cloud screening for Sun photometer aerosol optical depth (AOD) measurements. *Atmospheric Measurement Techniques, 12*(1).

Huang, J., Kondragunta, S., Laszlo, I., Liu, H., Remer, L. A., Zhang, H., et al. (2016). Validation and expected error estimation of Suomi-NPP VIIRS aerosol optical thickness and Ångström exponent with AERONET. Journal of Geophysical Research: Atmospheres, 121(12), 7139-7160. https://agupubs.onlinelibrary.wiley.com/doi/abs/10.1002/2016JD024834

Heymann, D. L. (2008). *Control of communicable diseases manual*: American Public Health Association.

Hou, W., Wang, J., Xu, X., & Reid, J. S. (2017). An algorithm for hyperspectral remote sensing of aerosols: 2. Information content analysis for aerosol parameters and principal components of surface spectra. *Journal of Quantitative Spectroscopy and Radiative Transfer, 192*, 14-29. http://www.sciencedirect.com/science/article/pii/S0022407316306604

Hsu, N. C., Lee, J., Sayer, A. M., Kim, W., Bettenhausen, C., & Tsay, S.-C. (2019). VIIRS Deep Blue Aerosol Products Over Land: Extending the EOS Long-Term Aerosol Data Records. *Journal of Geophysical Research: Atmospheres, 124*(7), 4026-4053. https://agupubs.onlinelibrary.wiley.com/doi/abs/10.1029/2018JD029688

Hsu, N. C., Si-Chee, T., King, M. D., & Herman, J. R. (2004). Aerosol properties over bright-reflecting source regions. *IEEE Transactions on Geoscience and Remote Sensing, 42*(3), 557-569.

Hu, X., Waller, L. A., Lyapustin, A., Wang, Y., Al-Hamdan, M. Z., Crosson, W. L., et al. (2014). Estimating ground-level PM2.5 concentrations in the Southeastern United States using MAIAC AOD retrievals and a two-stage model. *Remote Sensing of Environment, 140*, 220-232. http://www.sciencedirect.com/science/article/pii/S0034425713002903

Hu, Z. (2009). Spatial analysis of MODIS aerosol optical depth, PM2.5, and chronic coronary heart disease. *International Journal of Health Geographics, 8*(1), 27. https://doi.org/10.1186/1476-072X-8-27

975 Hu, Z., & Rao, K. R. (2009). Particulate air pollution and chronic ischemic heart disease in the
976 eastern United States: a county level ecological study using satellite aerosol data.
977 *Environmental Health, 8*(1), 26. https://doi.org/10.1186/1476-069X-8-26
978 Huff, A. K., Kondragunta, S., Zhang, H., Laszlo, I., Zhou, M., Caicedo, V., et al. (2021).
979 Tracking Smoke from a Prescribed Fire and its Impacts on Local Air Quality using
980 Temporally Resolved GOES-16 ABI Aerosol Optical Depth (AOD). *Journal of*
981 *Atmospheric and Oceanic Technology*.
982 https://journals.ametsoc.org/view/journals/atot/aop/JTECH-D-20-0162.1/JTECH-D-20-
983 0162.1.xml
984 Jackson, J. M., Liu, H., Laszlo, I., Kondragunta, S., Remer, L. A., Huang, J., & Huang, H. C.
985 (2013). Suomi-NPP VIIRS aerosol algorithms and data products. Journal of Geophysical
986 Research: Atmospheres, 118(22), 12,673-612,689.
987 Johnson, R. S., Zhang, J., Hyer, E. J., Miller, S. D., & Reid, J. S. (2013). Preliminary
988 investigations toward nighttime aerosol optical depth retrievals from the VIIRS
989 Day/Night Band. Atmos. Meas. Tech., 6(5), 1245-1255. https://www.atmos-meas-
990 tech.net/6/1245/2013/
991 Kessner, A. L., Wang, J., Levy, R. C., & Colarco, P. R. (2013). Remote sensing of surface
992 visibility from space: A look at the United States East Coast. *Atmospheric Environment,*
993 *81*, 136-147.
994 Kloog, I., Koutrakis, P., Coull, B. A., Lee, H. J., & Schwartz, J. (2011). Assessing temporally
995 and spatially resolved PM2.5 exposures for epidemiological studies using satellite aerosol
996 optical depth measurements. *Atmospheric Environment, 45*(35), 6267-6275.
997 http://www.sciencedirect.com/science/article/pii/S1352231011009125

998 Kokhanovsky, A. (2019). *Springer Series in Light Scattering: Volume 4: Light Scattering and*
999 *Radiative Transfer*: Springer.
1000 Konya, K., Yamaguchi, M., Takigawa, M., Miyakawa, T., & O'Neel, S. (2021). Mass
1001 concentration and origin of black carbon in spring snow on glaciers in the Alaska Range.
1002 Polar Science, 27, 100572.
1003 https://www.sciencedirect.com/science/article/pii/S1873965220300815
1004 Kopp, T. J., Thomas, W., Heidinger, A. K., Botambekov, D., Frey, R. A., Hutchison, K. D., et al.
1005 (2014). The VIIRS Cloud Mask: Progress in the first year of S-NPP toward a common
1006 cloud detection scheme. *Journal of Geophysical Research: Atmospheres, 119*(5), 2441-
1007 2456. https://agupubs.onlinelibrary.wiley.com/doi/abs/10.1002/2013JD020458
1008 Lee, J., Kim, J., Song, C. H., Ryu, J.-H., Ahn, Y.-H., & Song, C. K. (2010). Algorithm for
1009 retrieval of aerosol optical properties over the ocean from the Geostationary Ocean Color
1010 Imager. *Remote Sensing of Environment, 114*(5), 1077-1088.
1011 http://www.sciencedirect.com/science/article/pii/S0034425709003770
1012 Lei, N., Xiong, X., Wang, Z., Li, S., & Twedt, K. (2020). SNPP VIIRS RSB on-orbit radiometric
1013 calibration algorithms Version 2.0 and the performances, part 2: the performances.
1014 *Journal of Applied Remote Sensing, 14*(4), 047502.
1015 Lennartson, E. M., Wang, J., Gu, J., Castro Garcia, L., Ge, C., Gao, M., et al. (2018). Diurnal
1016 variation of aerosol optical depth and PM2.5 in South Korea: a synthesis from
1017 AERONET, satellite (GOCI), KORUS-AQ observation, and the WRF-Chem model.
1018 *Atmos. Chem. Phys., 18*(20), 15125-15144.
1019 https://acp.copernicus.org/articles/18/15125/2018/

1020 Levy, R. C., Remer, L. A., Tanré, D., Kaufman, Y. J., Ichoku, C., Holben, B. N., et al. (2003).
1021 Evaluation of the Moderate-Resolution Imaging Spectroradiometer (MODIS) retrievals
1022 of dust aerosol over the ocean during PRIDE. *Journal of Geophysical Research:*
1023 *Atmospheres, 108*(D19).
1024 https://agupubs.onlinelibrary.wiley.com/doi/abs/10.1029/2002JD002460
1025 Li, J., Carlson, B. E., & Lacis, A. A. (2015). How well do satellite AOD observations represent
1026 the spatial and temporal variability of PM2.5 concentration for the United States?
1027 *Atmospheric Environment, 102*, 260-273.
1028 https://www.sciencedirect.com/science/article/pii/S1352231014009583
1029 Li, Z., Li, K., Li, D., Yang, J., Xu, H., Goloub, P., & Victori, S. (2016). Simple transfer
1030 calibration method for a Cimel Sun–Moon photometer: calculating lunar calibration
1031 coefficients from Sun calibration constants. *Applied Optics, 55*(27), 7624-7630.
1032 http://ao.osa.org/abstract.cfm?URI=ao-55-27-7624
1033 Liao, L. B., Stephanie, W., Steve, M., & Bruce, H. (2013). Suomi NPP VIIRS day-night band
1034 on-orbit performance. *Journal of Geophysical Research: Atmospheres, 118*(22), 12,705-
1035 712,718. https://agupubs.onlinelibrary.wiley.com/doi/abs/10.1002/2013JD020475
1036 Liu, H., Laszlo, I., Ciren, P., Zhou, M., & Kondragunta, S. (2008, 7-11 July 2008). An
1037 Evaluation of the GOES-R ABI Aerosol Retrieval Algorithm. Paper presented at the
1038 IGARSS 2008 - 2008 IEEE International Geoscience and Remote Sensing Symposium.
1039 Liu, H., Remer, L. A., Huang, J., Huang, H. C., Kondragunta, S., Laszlo, I., et al. (2014).
1040 Preliminary evaluation of S-NPP VIIRS aerosol optical thickness. *Journal of*
1041 *Geophysical Research: Atmospheres, 119*(7), 3942-3962.

1042 Lyapustin, A., Wang, Y., Laszlo, I., Kahn, R., Korkin, S., Remer, L., et al. (2011). Multiangle
1043 implementation of atmospheric correction (MAIAC): 2. Aerosol algorithm. *Journal of*
1044 *Geophysical Research: Atmospheres, 116*(D3).
1045 https://agupubs.onlinelibrary.wiley.com/doi/abs/10.1029/2010JD014986
1046 Miller, S. D., Straka, W., Mills, S. P., Elvidge, C. D., Lee, T. F., Solbrig, J., et al. (2013).
1047 Illuminating the Capabilities of the Suomi National Polar-Orbiting Partnership (NPP)
1048 Visible Infrared Imaging Radiometer Suite (VIIRS) Day/Night Band. *Remote Sensing,*
1049 *5*(12), 6717-6766. https://www.mdpi.com/2072-4292/5/12/6717
1050 Miller, S. D., & Turner, R. E. (2009). A dynamic lunar spectral irradiance data set for
1051 NPOESS/VIIRS day/night band nighttime environmental applications. *IEEE*
1052 *Transactions on Geoscience and Remote Sensing, 47*(7), 2316-2329.
1053 Mills, S., Weiss, S., & Liang, C. (2013). *VIIRS day/night band (DNB) stray light*
1054 *characterization and correction.* Paper presented at the Earth Observing Systems XVIII.
1055 Myhre, G., Shindell, D., Bréon, F.-M., Collins, W., Fuglestvedt, J., Huang, J., et al. (2013).
1056 Anthropogenic and Natural Radiative Forcing. In T. F. Stocker, D. Qin, G.-K. Plattner,
1057 M. Tignor, S. K. Allen, J. Boschung, A. Nauels, Y. Xia, V. Bex, & P. M. Midgley (Eds.),
1058 *Climate Change 2013: The Physical Science Basis. Contribution of Working Group I to*
1059 *the Fifth Assessment Report of the Intergovernmental Panel on Climate Change* (pp.
1060 659–740). Cambridge, United Kingdom and New York, NY, USA: Cambridge
1061 University Press.
1062 Omar, A. H., Won, J. G., Winker, D. M., Yoon, S. C., Dubovik, O., & McCormick, M. P.
1063 (2005). Development of global aerosol models using cluster analysis of Aerosol Robotic

1064 Network (AERONET) measurements. *Journal of Geophysical Research: Atmospheres,*
1065 *110*(D10).
1066 Polivka, T. N., Hyer, E. J., Wang, J., & Peterson, D. A. (2015). First Global Analysis of
1067 Saturation Artifacts in the VIIRS Infrared Channels and the Effects of Sample
1068 Aggregation. *IEEE Geoscience and Remote Sensing Letters, 12*(6), 1262-1266.
1069 Polivka, T. N., Wang, J., Ellison, L. T., Hyer, E. J., & Ichoku, C. M. (2016). Improving
1070 Nocturnal Fire Detection With the VIIRS Day–Night Band. *IEEE Transactions on*
1071 *Geoscience and Remote Sensing, 54*(9), 5503-5519.
1072 Pope, C. A., & Dockery, D. W. (2006). Health Effects of Fine Particulate Air Pollution: Lines
1073 that Connect. *Journal of the Air & Waste Management Association, 56*(6), 709-742.
1074 https://doi.org/10.1080/10473289.2006.10464485
1075 Pöschl, U. (2005). Atmospheric aerosols: composition, transformation, climate and health
1076 effects. *Angewandte Chemie International Edition, 44*(46), 7520-7540.
1077 Randles, C. A., da Silva, A. M., Buchard, V., Colarco, P. R., Darmenov, A., Govindaraju, R., et
1078 al. (2017). The MERRA-2 Aerosol Reanalysis, 1980 Onward. Part I: System Description
1079 and Data Assimilation Evaluation. *Journal of Climate, 30*(17), 6823-6850.
1080 https://journals.ametsoc.org/view/journals/clim/30/17/jcli-d-16-0609.1.xml
1081 Reid, J. S., Kuehn, R. E., Holz, R. E., Eloranta, E. W., Kaku, K. C., Kuang, S., et al. (2017).
1082 Ground-based High Spectral Resolution Lidar observation of aerosol vertical distribution
1083 in the summertime Southeast United States. *Journal of Geophysical Research:*
1084 *Atmospheres, 122*(5), 2970-3004.
1085 https://agupubs.onlinelibrary.wiley.com/doi/abs/10.1002/2016JD025798

1086 Remer, L. A., Kaufman, Y., Tanré, D., Mattoo, S., Chu, D., Martins, J. V., et al. (2005). The
1087 MODIS aerosol algorithm, products, and validation. *Journal of the atmospheric sciences,*
1088 *62*(4), 947-973.
1089 Román, M. O., Wang, Z., Sun, Q., Kalb, V., Miller, S. D., Molthan, A., et al. (2018). NASA's
1090 Black Marble nighttime lights product suite. *Remote Sensing of Environment, 210*, 113-
1091 143. http://www.sciencedirect.com/science/article/pii/S003442571830110X
1092 Saunders, R. (1986). An automated scheme for the removal of cloud contamination from
1093 AVHRR radiances over western Europe. *International Journal of Remote Sensing, 7*(7),
1094 867-886.
1095 Saunders, R. W., & Kriebel, K. T. (1988). An improved method for detecting clear sky and
1096 cloudy radiances from AVHRR data. *International Journal of Remote Sensing, 9*(1), 123-
1097 150. https://doi.org/10.1080/01431168808954841
1098 Sawyer, V., Levy, R. C., Mattoo, S., Cureton, G., Shi, Y., & Remer, L. A. (2020). Continuing the
1099 MODIS Dark Target Aerosol Time Series with VIIRS. *Remote Sensing, 12*(2), 308.
1100 https://www.mdpi.com/2072-4292/12/2/308
1101 Schlyter, P. (2010). Computing planetary positions-a tutorial with worked examples.
1102 *Downloaded March, 26*, 2010.
1103 Sekiyama, T. T., Tanaka, T. Y., Shimizu, A., & Miyoshi, T. (2010). Data assimilation of
1104 CALIPSO aerosol observations. *Atmos. Chem. Phys., 10*(1), 39-49. https://www.atmos-
1105 chem-phys.net/10/39/2010/
1106 Sessions, W. R., Reid, J. S., Benedetti, A., Colarco, P. R., da Silva, A., Lu, S., et al. (2015).
1107 Development towards a global operational aerosol consensus: basic climatological
1108 characteristics of the International Cooperative for Aerosol Prediction Multi-Model

Ensemble (ICAP-MME). *Atmos. Chem. Phys., 15*(1), 335-362. https://acp.copernicus.org/articles/15/335/2015/

Shao, X., Cao, C., Liu, T.-C., Uprety, S., Zhang, B., Wang, W., & Blonski, S. (2018). *Characterization and correction of stray light for NOAA-20 VIIRS day/night band.* Paper presented at the Earth Observing Missions and Sensors: Development, Implementation, and Characterization V.

Singh, J., Noh, Y.-J., Agrawal, S., & Tyagi, B. (2019). Dust detection and aerosol properties over arabian sea using MODIS data. *Earth Systems and Environment, 3*(1), 139-152.

Sinyuk, A., Holben, B. N., Eck, T. F., Giles, D. M., Slutsker, I., Korkin, S., et al. (2020). The AERONET Version 3 aerosol retrieval algorithm, associated uncertainties and comparisons to Version 2. *Atmos. Meas. Tech., 13*(6), 3375-3411. https://amt.copernicus.org/articles/13/3375/2020/

Spurr, R., & Christi, M. (2019). The LIDORT and VLIDORT linearized scalar and vector discrete ordinate radiative transfer models: updates in the last 10 years. In *Springer Series in Light Scattering* (pp. 1-62): Springer.

Spurr, R., Wang, J., Zeng, J., & Mishchenko, M. I. (2012). Linearized T-matrix and Mie scattering computations. *Journal of Quantitative Spectroscopy and Radiative Transfer, 113*(6), 425-439. http://www.sciencedirect.com/science/article/pii/S0022407311004006

Thieuleux, F., Moulin, C., Breon, F.-M., Maignan, F., Poitou, J., & Tanré, D. (2005). Remote sensing of aerosols over the oceans using MSG/SEVIRI imagery. *Annales Geophysicae, 23*(12), 3561-3568. https://hal.archives-ouvertes.fr/hal-00330068

van Donkelaar, A., Martin, R. V., & Park, R. J. (2006). Estimating ground-level PM2.5 using aerosol optical depth determined from satellite remote sensing. *Journal of Geophysical*

Research: Atmospheres, 111(D21). https://agupubs.onlinelibrary.wiley.com/doi/abs/10.1029/2005JD006996

Wang, J., Aegerter, C., Xu, X., & Szykman, J. J. (2016). Potential application of VIIRS Day/Night Band for monitoring nighttime surface PM2.5 air quality from space. *Atmospheric Environment, 124*, 55-63.

Wang, J., & Christopher, S. A. (2003). Intercomparison between satellite-derived aerosol optical thickness and PM2.5 mass: Implications for air quality studies. *Geophysical Research Letters, 30*(21). https://agupubs.onlinelibrary.wiley.com/doi/abs/10.1029/2003GL018174

Wang, J., Christopher, S. A., Brechtel, F., Kim, J., Schmid, B., Redemann, J., et al. (2003a). Geostationary satellite retrievals of aerosol optical thickness during ACE-Asia. *Journal of Geophysical Research: Atmospheres, 108*(D23). https://agupubs.onlinelibrary.wiley.com/doi/abs/10.1029/2003JD003580

Wang, J., Christopher, S. A., Reid, J. S., Maring, H., Savoie, D., Holben, B. N., et al. (2003b). GOES 8 retrieval of dust aerosol optical thickness over the Atlantic Ocean during PRIDE. *Journal of Geophysical Research: Atmospheres, 108*(D19). https://agupubs.onlinelibrary.wiley.com/doi/abs/10.1029/2002JD002494

Wang, J., Nair, U., & Christopher, S. A. (2004). GOES-8 aerosol optical thickness assimilation in a mesoscale model: Online integration of aerosol radiative effects. *J. Geophys. Res., 109*, D23203, doi:23210.21029/22004JD004827.

Wang, J., Park, S., Zeng, J., Ge, C., Yang, K., Carn, S., et al. (2013). Modeling of 2008 Kasatochi volcanic sulfate direct radiative forcing: assimilation of OMI SO₂ plume height data and comparison with MODIS and CALIOP observations. *Atmos. Chem. Phys., 13*(4), 1895-1912. https://www.atmos-chem-phys.net/13/1895/2013/

Wang, J., Roudini, S., Hyer, E. J., Xu, X., Zhou, M., Garcia, L. C., et al. (2020a). Detecting nighttime fire combustion phase by hybrid application of visible and infrared radiation from Suomi NPP VIIRS. Remote Sensing of Environment, 237, 111466. http://www.sciencedirect.com/science/article/pii/S0034425719304857

Wang, J., Xu, X., Ding, S., Zeng, J., Spurr, R., Liu, X., et al. (2014). A numerical testbed for remote sensing of aerosols, and its demonstration for evaluating retrieval synergy from a geostationary satellite constellation of GEO-CAPE and GOES-R. *Journal of Quantitative Spectroscopy and Radiative Transfer, 146*, 510-528. http://www.sciencedirect.com/science/article/pii/S0022407314001368

Wang, J., Xu, X., Henze, D. K., Zeng, J., Ji, Q., Tsay, S.-C., & Huang, J. (2012). Top-down estimate of dust emissions through integration of MODIS and MISR aerosol retrievals with the GEOS-Chem adjoint model. *Geophysical Research Letters, 39*(8), L08802. http://dx.doi.org/10.1029/2012GL051136

Wang, J., Zhou, M., Xu, X., Roudini, S., Sander, S. P., Pongetti, T. J., et al. (2020b). Development of a nighttime shortwave radiative transfer model for remote sensing of nocturnal aerosols and fires from VIIRS. *Remote Sensing of Environment, 241*, 111727. http://www.sciencedirect.com/science/article/pii/S0034425720300973

Wang, Y., Wang, J., Levy, R. C., Xu, X., & Reid, J. S. (2017). MODIS Retrieval of Aerosol Optical Depth over Turbid Coastal Water. *Remote Sensing, 9*(6), 595.

Wanner, W., Li, X., & Strahler, A. H. (1995). On the derivation of kernels for kernel-driven models of bidirectional reflectance. *Journal of Geophysical Research: Atmospheres, 100*(D10), 21077-21089. http://dx.doi.org/10.1029/95JD02371

1177 Wolfe, R. E., Lin, G., Nishihama, M., Tewari, K. P., Tilton, J. C., & Isaacman, A. R. (2013).
1178 Suomi NPP VIIRS prelaunch and on-orbit geometric calibration and characterization.
1179 *Journal of Geophysical Research: Atmospheres, 118*(20).
1180 Xian, P., Reid, J. S., Hyer, E. J., Sampson, C. R., Rubin, J. I., Ades, M., et al. (2019). Current
1181 state of the global operational aerosol multi-model ensemble: An update from the
1182 International Cooperative for Aerosol Prediction (ICAP). *Quarterly Journal of the Royal*
1183 *Meteorological Society, 145*(S1), 176-209.
1184 https://rmets.onlinelibrary.wiley.com/doi/abs/10.1002/qj.3497
1185 Xu, X., & Wang, J. (2015). Retrieval of aerosol microphysical properties from AERONET
1186 photopolarimetric measurements: 1. Information content analysis. *Journal of Geophysical*
1187 *Research: Atmospheres, 120*(14), 7059-7078.
1188 https://agupubs.onlinelibrary.wiley.com/doi/abs/10.1002/2015JD023108
1189 Xu, X., Wang, J., Henze, D. K., Qu, W., & Kopacz, M. (2013). Constraints on aerosol sources
1190 using GEOS-Chem adjoint and MODIS radiances, and evaluation with multisensor
1191 (OMI, MISR) data. *Journal of Geophysical Research: Atmospheres, 118*, 6396-6413.
1192 http://dx.doi.org/10.1002/jgrd.50515
1193 Xu, X., Wang, J., Wang, Y., Zeng, J., Torres, O., Reid, J. S., et al. (2019). Detecting layer height
1194 of smoke aerosols over vegetated land and water surfaces via oxygen absorption bands:
1195 hourly results from EPIC/DSCOVR in deep space. *Atmos. Meas. Tech., 12*(6), 3269-
1196 3288. https://www.atmos-meas-tech.net/12/3269/2019/
1197 Xu, X., Wang, J., Zeng, J., Spurr, R., Liu, X., Oleg, D., et al. (2015). Retrieval of aerosol
1198 microphysical properties from AERONET photopolarimetric measurements: 2. A new
1199 research algorithm and case demonstration. *Journal of Geophysical Research:*

Atmospheres, 120(14), 7079-7098. https://agupubs.onlinelibrary.wiley.com/doi/abs/10.1002/2015JD023113

Zhang, H., Lyapustin, A., Wang, Y., Kondragunta, S., Laszlo, I., Ciren, P., & Hoff, R. M. (2011). A multi-angle aerosol optical depth retrieval algorithm for geostationary satellite data over the United States. *Atmos. Chem. Phys., 11*(23), 11977-11991. https://www.atmos-chem-phys.net/11/11977/2011/

Zhang, H., Hoff, R. M., Kondragunta, S., Laszlo, I., & Lyapustin, A. (2013). Aerosol optical depth (AOD) retrieval using simultaneous GOES-East and GOES-West reflected radiances over the western United States. Atmos. Meas. Tech., 6(2), 471-486. https://amt.copernicus.org/articles/6/471/2013/

Zhang, J., Jaker, S. L., Reid, J. S., Miller, S. D., Solbrig, J., & Toth, T. D. (2019). Characterization and application of artificial light sources for nighttime aerosol optical depth retrievals using the Visible Infrared Imager Radiometer Suite Day/Night Band. *Atmos. Meas. Tech., 12*(6), 3209-3222. https://www.atmos-meas-tech.net/12/3209/2019/

Zhang, J., Reid, J. S., Westphal, D. L., Baker, N. L., & Hyer, E. J. (2008). A system for operational aerosol optical depth data assimilation over global oceans. *Journal of Geophysical Research: Atmospheres, 113*(D10). https://agupubs.onlinelibrary.wiley.com/doi/abs/10.1029/2007JD009065

Zhang, W., Xu, H., & Zheng, F. (2018). Aerosol Optical Depth Retrieval over East Asia Using Himawari-8/AHI Data. *Remote Sensing, 10*(1), 137. https://www.mdpi.com/2072-4292/10/1/137